INSTITUT DE FRANCE
Académie des sciences

Comptes Rendus

Géoscience

Sciences de la Planète

Joan Andújar, Bruno Scaillet, Manuel Moreira, Ida Di Carlo, Anne Le Friant, Manon Bickert, Fabien Paquet, Stephan Jorry and Nathalie Feuillet

Experimental evidence for the shallow production of phonolitic magmas at Mayotte

Published online: 12 January 2023

https://doi.org/10.5802/crgeos.182

Part of Special Issue: The Mayotte seismo-volcanic crisis of 2018-2021 in the Comoros archipelago (Mozambique channel)

Guest editors: Jérôme Van der Woerd (Institut Terre Environnement de Strabourg, UMR 7063 CNRS / Université de Strasbourg, 67084 Strasbourg, France), Vincent Famin (Laboratoire Géosciences Réunion, Université de La Réunion - IPGP, 97744 Saint-Denis, France) and Eric Humler (Professeur Université de Nantes, Laboratoire de Planétologie et Géosciences, UMR 6112, Faculté des Sciences et Techniques, Nantes Université, 44322 Nante, France)

This article is licensed under the
Creative Commons Attribution 4.0 International License.
http://creativecommons.org/licenses/by/4.0/

Les Comptes Rendus. Géoscience — Sciences de la Planète *sont membres du Centre Mersenne pour l'édition scientifique ouverte*
www.centre-mersenne.org
e-ISSN : 1778-7025

Comptes Rendus
Géoscience — Sciences de la Planète
Published online: 12 January 2023
https://doi.org/10.5802/crgeos.182

The Mayotte seismo-volcanic crisis of 2018-2021 in the Comoros archipelago (Mozambique channel) / *La crise sismo-volcanique de 2018-2021 de Mayotte dans l'archipel des Comores (Canal du Mozambique)*

Experimental evidence for the shallow production of phonolitic magmas at Mayotte

Evidence expérimentale de la production de magmas phonolitiques à faible profondeur à Mayotte

Joan Andújar [*, a], **Bruno Scaillet** [a], **Manuel Moreira** [a], **Ida Di Carlo** [a], **Anne Le Friant** [b], **Manon Bickert** [c], **Fabien Paquet** [d], **Stephan Jorry** [e] **and Nathalie Feuillet** [b]

[a] Institut des Sciences de la Terre d'Orléans (ISTO), UMR 7327, Université d'Orléans, CNRS, BRGM, 1A rue de la Férollerie, F-45071 Orléans, France

[b] Université de Paris, Institut de physique du globe de Paris, CNRS, F-75005 Paris, France

[c] Dipartimento di Scienze Chimiche e Geologiche, Università di Modena e Reggio Emilia, Modena, Italy

[d] BRGM-French geological survey, DGR/GBS, 3 avenue Claude Guillemin, BP36009, F-45060 Orleans Cedex 2, France

[e] Geo-Ocean, Univ Brest, Ifremer, CNRS, Technopole La Pointe du Diable, 29280 Plouzané, France

E-mails: juan.andujar@cnrs-orleans.fr (J. Andújar), bscaille@cnrs-orleans.fr (B. Scaillet), manuel.moreira@cnrs-orleans.fr (M. Moreira), ida.di-carlo@cnrs-orleans.fr (I. Di Carlo), Lefriant@ipgp.fr (A. Le Friant), manon.bickert@gmail.com (M. Bickert), F.Paquet@brgm.fr (F. Paquet), Stephan.Jorry@ifremer.fr (S. Jorry), feuillet@ipgp.fr (N. Feuillet)

Abstract. Since May 2018 till the end of 2021, Mayotte island has been the locus of a major submarine volcanic eruption characterized by the offshore emission of more than 6.5 km^3 of basanitic magma. The eruption occurred along a WNW–ESE trending submarine ridge on the east flank of the island where, in addition, several seemingly recent phonolitic bodies were also identified close to the island. To define realistic scenarios of magma ascent and potentially predict the style of an upcoming event, it is crucial to have a precise understanding on the plumbing system operating below volcanoes. The putative relationships between basanites emitted by the new volcano and these recent phonolites have been experimentally explored by performing crystallization experiments on a representative basanite over a large range of pressures (up to

* Corresponding author.

400 MPa). The results show that the crystallization of basanite at crustal levels (≤12–15 km) yields a phonolitic residual liquid containing up to 3–4 wt% H_2O after ≥65 wt% of an assemblage of olivine+plagioclase+amphibole+clinopyroxene+biotite+magnetite+ilmenite+apatite. The final iron content of the residual phonolitic liquids is strongly controlled by the depth/pressure of fractionation. Fe-rich phonolites from the submarine ridge are produced at 6–8 km depth, while a shallower differentiation (≤4–5 km) results in the production of liquids with trachyte–benmoreite affinities. If the fractionation process occurs at depths higher than 8 km, the resulting phonolitic melts are progressively enriched in SiO_2–Al_2O_3 but depleted in FeO*, ie unlike those erupted. We therefore conclude that phonolitic magma production and storage at Mayotte is a rather shallow process.

Résumé. Depuis mai 2018 et jusqu'à la fin de l'année 2021, l'île de Mayotte a été le scenario d'une éruption volcanique sous-marine majeure caractérisée par l'émission en mer de plus de 6,5 km^3 de magma basanitique. L'éruption s'est produite le long d'une ride sous-marine orientée ONO–ESE sur le flanc est de l'île où, entre autre, plusieurs corps phonolitiques d' aspect récent ont également été identifiés à proximité de l'île. Pour définir des scénarios réalistes d'ascension du magma et potentiellement prévoir le style d'un événement à venir, il est crucial d'avoir une compréhension précise du système de plomberie magmatique opérant sous les volcans. Les relations génétiques potentielles entre les basanites émises par le nouveau volcan et ces phonolites récentes ont été explorées expérimentalement en effectuant des expériences de cristallisation sur une basanite représentative, et ce sur une large gamme de pressions (jusqu'à 400 MPa). Les résultats montrent que la cristallisation de la basanite à des profondeurs crustales (≤12–15 km) produit un liquide résiduel phonolitique contenant jusqu'à 3–4 % en poids (pd.%) de H_2O, après la précipitation d'au moins 65 pd.% d'un assemblage d'olivine+plagioclase+amphibole+clinopyroxène+biotite+magnétite+ilménite+apatite. La teneur finale en fer des liquides phonolitiques résiduels est fortement contrôlée par la profondeur/pression de cristallisation. Les phonolites riches en fer de la dorsale sous-marine sont produites à 6–8 km de profondeur, tandis qu'une différenciation moins profonde (≤4–5 km) entraîne la production de liquides à affinités trachyte–benmoreite. Si le processus de fractionnement se produit à des profondeurs supérieures à 8 km, les liquides phonolitiques résultants sont progressivement enrichis en SiO_2–Al_2O_3 mais appauvris en FeO*, c'est-à-dire différents des phonolites naturelles. Nous concluons donc que la production et le stockage de magma phonolitique à Mayotte est un processus plutôt superficiel.

Keywords. Mayotte, Phase equilibria, Phonolite, Iron-enrichment, Basanite.

Mots-clés. Mayotte, Equilibres de phases, Phonolite, Enrichement en fer, Basanite.

Published online: 12 January 2023

1. Introduction

Understanding the plumbing systems feeding volcanic eruptions is critical for providing an accurate interpretation of the different signals (seismicity, surface deformation, gas emissions) generated during periods of volcanic reactivation or eruption. Having accurate constraints on magma temperature, storage depths and on the amount of volatiles (H_2O, CO_2, S, F, Cl… etc.) dissolved in the magma allow to define more realistic scenarios for simulating the ascent and potentially predict the style of the upcoming event. In systems where different types of magmas (i.e., mafic to felsic) are emitted, an important question is to understand under which conditions basaltic melts evolve towards felsic compositions, and in particular whether this process occurs in a single or in multiple reservoirs located at different depths. This is crucial for understanding the final storage level of more evolved compositions and the structure of the plumbing system beneath a volcano, as the generation level of the felsic melts may not correspond to that of their pre-eruptive storage. In this contribution, we address this issue by unravelling the parental relationships between recent erupted basanites and phonolites at Mayotte (North Mozambique channel) using an experimental approach.

Between May 2018 and the end of 2021, Mayotte island has experienced a major submarine volcanic eruption characterized by the emission of more than 6.55 km^3 of magma [Feuillet, 2019, ReVoSiMa, 2022]. Prior to this event, the island has not experienced historical episodes of reactivation, and the latest known volcanic event occurred some 7000 yrs ago on Petite Terre [Zinke et al., 2003]. The 2018–2021 eruption occurred along a WNW–ESE trending submarine ridge on the east flank of the island (Figure 1).

Two main seismic swarms are still active below the ridge: a proximal and a distal cluster [Bertil et al., 2021, Cesca et al., 2020, Feuillet et al., 2021,

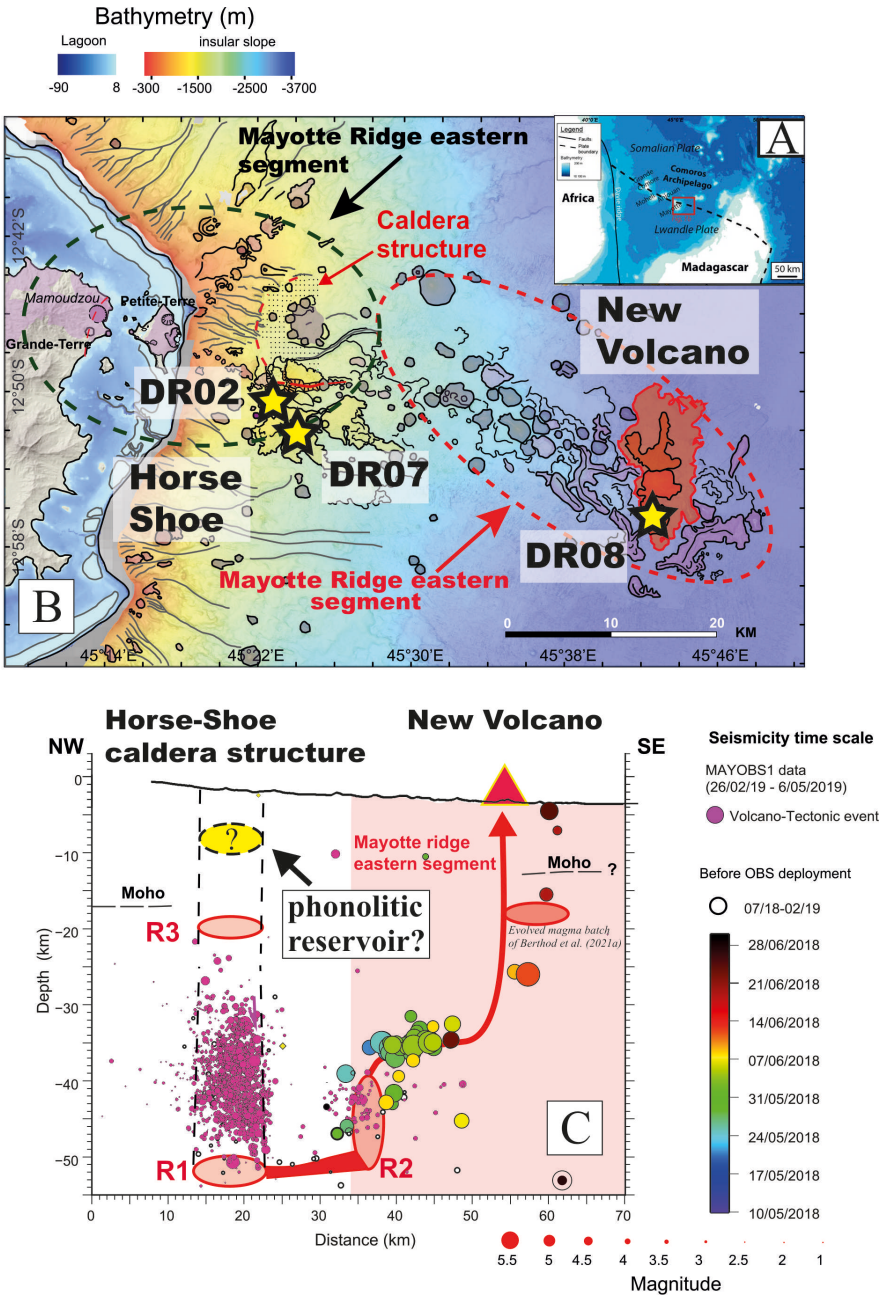

Figure 1. (A) Location of Comoros archipelago in the Mozambique channel. (B) Geological map of the active submarine volcanic ridge at Mayotte (modified from Feuillet et al. [2021]) showing the locations of the new volcano, and the Horse-shoe zone having active submarine degassing. The location of the dredged samples considered in this study is marked by yellow stars (modified from Berthod et al. [2021b]). (C) Depth distribution of the two well identified seismic swarms over the submarine ridge of Mayotte (modified from Feuillet et al. [2021]). The three seismically active zones R1, R2, R3 identified during this eruption, and the petrologically inferred reservoir located below the volcano and intercepted by the rising magma, are also shown [Feuillet et al., 2021, Foix et al., 2021 and Berthod et al., 2021b]. The emptying of a potential shallow phonolitic reservoir, as inferred in this work, could have produced the Horseshoe structure (see text for details).

Lavayssière et al., 2022, Lemoine et al., 2020, Saurel et al., 2021]. The distal cluster is located 30 km far from the eastern coast of Petite Terre whereas the proximal one is much closer (5–10 km from Petite Terre). Feuillet et al. [2021] inferred that the distal swarm was promoted by the drainage and consecutive stress changes around a ~40 km deep magmatic reservoir (R2). Relocations of seismic events recorded by seismic stations onshore within the first weeks of the crisis show that a dike propagated from this reservoir R2 to transport the magma toward the seafloor at the eruption site [Feuillet et al., 2021]. Following the eruption, the proximal cluster was activated likely following the drainage of deeper (55 km) reservoir R1 and the consecutive collapse of a deep caldera structure above [Feuillet et al., 2021]. The proximal cluster is located below an old caldera structure where sits the Horseshoe zone [Figures 1B–C, Feuillet et al., 2021]. Active degassing is observed in this zone, giving rise to submarine plumes but without emission of fresh lava [Feuillet et al., 2021]. Ground deformation modeling revealed the drainage of about 5 km^3 of a deep -seated reservoir [Lemoine et al., 2020], inferred to be R2 [Feuillet et al., 2021].

Recent passive tomography data [Foix et al., 2021], along with the detection of an important number of very low frequency events at ~20 km [VLF; Laurent et al., 2021], suggest the presence of a third reservoir (R3; Figure 1C) above the deep caldera structure. The reactivation of this reservoir could be at the origin of the gas-emissions observed on the horseshoe region [Foix et al., 2021].

Geothermobarometry calculations broadly support the above seismic depths for the deep reservoirs (volume ≥ 10 km^3; depths ≥ 37 km), in which the hydrous (2.3 wt% H_2O dissolved in melt, H_2O_{melt}) evolved basanite (generated by ~50% of crystallization of a more primitive magma; Berthod et al. [2021a]) was sourced. Berthod et al. [2021a] further proposed that during its uprise, the basanite intercepted a shallower pre-existing reservoir at 17 ± 6.5 km below the new volcano (Figure 1C), in which a more evolved magma originated during recent magmatic episodes was residing.

The appearance of the dense seismic swarm beneath the Horseshoe region (Figure 1C) and the discovery of intensive submarine gas plumes, prompted the community for sampling this zone located 15 km away from Petite Terre. The study of samples dredged in this area revealed the presence of a bimodal compositional distribution of the emitted magmas in contrast to the new volcano, where basanite flows predominate. Within the Horseshoe region, several phonolitic bodies occur in abundance in addition to basanites, outcropping on the caldera borders and flowing downwards (Figure 1B; Berthod et al. [2021a,b]). The possible genetic link between the submarine basanites and phonolites was explored in Berthod et al. [2021b] through fractional crystallization modelling of major and trace elements along with Rhyolite-MELTs simulations [Ghiorso and Gualda, 2015]. These modelling results show that the production of phonolite liquids from a hydrous (2.3 wt% H_2O_{melt}) basanite requires 80% of fractional crystallization of a mineral assemblage consisting of clinopyroxene (Cpx), olivine (Ol), magnetite (Mt), apatite (Ap), ilmenite (Ilm) and anorthoclase alkali feldspar (Afs) at ≤1000 °C, $P \geq 600$ MPa and $fO_2 \sim$ FMQ-1. Cpx–Opx barometry performed on mantle xenoliths carried by both phonolitic and basanitic samples from the Horseshoe region, yields similar storage conditions (15–20 km; Figure 1C). Based on these lines of evidence, these authors conclude that crystallisation of evolved basanitic melts at low oxygen fugacity produced the erupted Fe-rich phonolitic melts at Moho levels [Dofal et al., 2021].

It is worth noting that most of the phonolitic magmas known worldwide evolve at relatively shallow conditions [$P \leq 200$ MPa or ≤6–8 km; Andújar et al., 2008, 2010, 2013, Berndt et al., 2001, Harms et al., 2004, Moussallam et al., 2013, Scaillet et al., 2008]. However, rare are the cases concerning mantle-xenolith bearing phonolites [e.g. Berthod et al., 2021b, Dautria et al., 1983]. At first sight, the presence of mantle fragments within phonolitic magmas, along with thermobarometric calculations, hint at a rapid ascent of these magmas from deep mantle levels. Yet, examples of mafic to intermediate magmas containing significant amounts of different types of mantle xenoliths are manifold in alkaline series [e.g., La Palma, Klügel et al., 1999, 2022, Lanzarote, Neumann et al., 1995, La Garrotxa, Spain, Pedrazzi et al., 2022]. Since the products and mineralogy of evolved phonolites often show evidence of mixing-mingling with more mafic melts [i.e. mixed pumices, presence of inverse zonations in feldspars, olivine; Andújar et al., 2013, Andújar and Scaillet, 2012, Berthod et al., 2021b, Wolff, 1985; among oth-

ers], the injection of mantle-bearing mafic magmas into phonolitic reservoirs could also account for the occurrence of these mantle fragments into the phonolites.

Another point worth of note is the use of thermobarometric equations [e.g., Putirka, 2008] along with thermodynamic algorithms like MELTS or Rhyolite-MELTS [Gualda et al., 2012] for retrieving the ponding conditions and/or modelling the crystallization behavior of felsic alkaline magmas. These thermobarometric calibrations have important associated uncertainties on intensive parameters, in particular P [e.g. ±50 °C for T and ±150–400 MPa for P or 5–12 km in depth; Berthod et al., 2021a,b, Putirka, 2008, 2016, Ubide et al., 2019] which limit their practical use in volcanological contexts, notably for inferring precisely storage conditions or comparing them to geophysical data. In particular, recent works have shown that amphibole- and Cpx- based geobarometers either do not capture real pressure [Erdmann et al., 2014] or overestimate considerably it [Hammer et al., 2016], in particular when applied to alkaline magmas [Hammer et al., 2016].

Similarly, while MELTs algorithm can faithfully simulate the evolution of anhydrous mafic melts at low pressures, the application of this model to the study of hydrous mafic melts is still limited, in large part because it cannot predict the crystallization of important hydrous phases such as amphibole or biotite. Significant differences in the crystallization temperatures and stability fields of phases like Cpx or Plagioclase in hydrous systems have also been reported [Freise et al., 2009, MacDonald et al., 2021].

Whereas the above approaches remain valuable for a first order evaluation of the ponding and evolution conditions of crystal-bearing magmas, the uncertainties and lack of calibration issues outlined above indicate that these methods are not standalone tools, and still need to be confronted to experimental results whenever possible. Accordingly, here we report experimental data gained on mafic magmas from Mayotte in order to put constraints on the generation conditions of phonolitic melts in this area.

2. Geological setting

Mayotte is the easternmost and oldest island of the Comoros archipelago, composed of a main volcanic island (Grande Terre) and a volcanic islet (Petite Terre) located 4 km away to the east (Figure 1B). Mayotte was constructed in three main different phases of volcanism: the first stage corresponds to the shield-building phase, between 20 and 3.8 Ma, followed by a fissure-erupted post erosional phase (3.8–2.5 Ma) and a final episode [2.4–1.5 Ma; Späth et al., 1996]. In detail, the volcanic activity of Grande Terre migrated from the southern part of the island during early stages (10.6–1.9 Ma) towards the north (5–0.75 Ma) and north-east (0.75–Present), with periods of quiescence in between [Debeuf, 2004, Nehlig et al., 2013]. This period of activity may also concern offshore WNW–ESE volcanic chains extending from Petite-Terre down to the newly discovered Fani Maore offshore volcano, Feuillet et al. [2021].

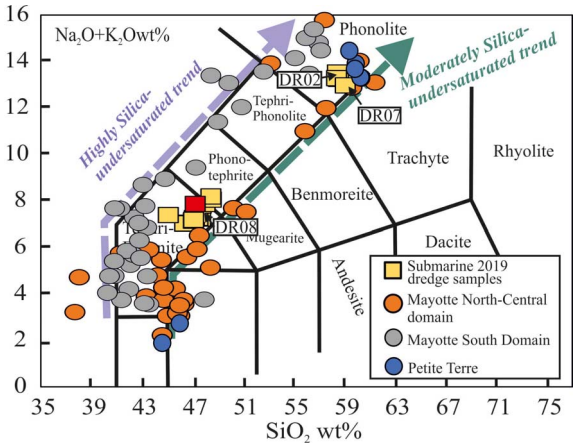

Figure 2. Total alkali ($Na_2O + K_2O$) versus SiO_2 diagram [TAS after Le Bas and Streckeisen, 1991] showing the two different liquid lines of descent of Mayotte magmas: highly silica-undersaturated and moderately silica-undersaturated trends. The products dredged on the active submarine ridge and those from Petite Terre are also shown. Compositional data are from Pelleter et al. [2014] and Berthod et al. [2021a,b].

The compositions of magmas erupted on Mayotte islands and along the 60 km of submarine ridge clearly define two distinct magmatic lineages. Whereas magmas from the southern Mayotte region are alkali-rich and highly silica undersaturated, those from north central-east sectors and the most recent Holocene products (including the 2018–2021 submarine eruption) are also silica-undersaturated but show a moderate alkali enrichment (Figure 2). Com-

positional differences between these two series are readily explained by the mineralogical heterogeneity of their source regions [Späth et al., 1996]. In both cases, crystal-fractionation has been proposed to be the main mechanism controlling magma evolution [Berthod et al., 2021a,b, Pelleter et al., 2014, Späth et al., 1996]. Despite their different sources, the magmas from these two series are dominated by the same mineralogy sensu latto. Ol+Cpx operate at the very initial stages of the fractionation process, being joined, and progressively replaced by, Fe–Ti oxides, feldspar and amphibole, as well as accessory amounts of apatite and titanite with increasing degrees of differentiation [Debeuf, 2004, Pelleter et al., 2014, Späth et al., 1996].

3. Experimental work

3.1. *Preparation of the starting material*

The starting material used for our experiments is the sample DR08 that was dredged during the early phases of the 2018–2021 eruption by the MAYOBS-2 oceanographic campaign [Figure 1B; Table 1; Jorry, 2019]. This sample has been petrologically characterized by Berthod et al. [2021a]; according to these authors (see their Tables 2–4), it is an evolved glassy popping-rock basanite (Mg ~ 4.5 wt%; Table 1) with normative olivine content being ≥10%, moderately vesicular (~31%) with 5–9% (calculated on a bubble-free basis) of olivine (~Fo72 ± 2 mol%), and trace amounts of Ti-magnetite and apatite.

Several pieces of this glassy rock were first finely ground in an agate mortar, put in a Pt crucible at 1400 °C and melted twice, with grinding in between, during 5 h in open atmosphere. Electron microprobe analyses (EMPA) of the starting glass show a homogeneous composition with no significant Na or Fe loss compared to data from Berthod et al. [2021a, Table 1]. The resulting dry glass was then ground to obtain the powder that was used as starting material for the phase equilibrium experiments and stored in an oven at 120 °C.

3.2. *Experimental equipment and strategy*

In total, six experiments were performed (Table 2) at the ISTO experimental laboratory, using the same experimental apparatus and procedure of Andújar et al. [2013], Moussallam et al. [2013], Scaillet et al. [1992], which are briefly summarized below. Experiments were carried out in an Internally Heated Pressure Vessel (IHPV) operating vertically, loaded with Ar–H_2 mixtures at room temperature to achieve the desired fO_2 conditions (see below). Total pressure was recorded by a transducer calibrated against a Heise Bourdon gauge with an uncertainty of ±20 bars. A double-winding kanthal furnace was used as this allows to achieve near-isothermal conditions (gradient <2–3 °C/cm) along a 3 cm long hot spot. Temperature was measured using K-type thermocouples with an accuracy of ±5 °C. A rapid-quench technique was systematically used, imparting isobaric cooling rates of >100 °C/s [e.g., Andújar et al., 2013, 2015, Scaillet et al., 2008]. In all runs reported here, the drop quench was successful as indicated by the rise in total pressure upon the falling of the sample holder into the cold (bottom) part of the vessel.

Experiments were mainly conducted at T–P conditions covering those determined for similar phonolites worldwide [e.g., Andújar et al., 2008, 2010, 2013, Andújar and Scaillet, 2012, Giehl et al., 2013, Moussallam et al., 2013, Scaillet et al., 2008]. Temperature was set at 925 and 950 °C whereas explored pressures were 100, 150, 200 and 400 MPa. Based on the iron-rich character of the Mayotte phonolites [Berthod et al., 2021b], the initial fO_2 was set at ≤ NNO buffer (where NNO refers to the Ni–NiO buffer) as Fe enrichment in magmas is favoured by low fO_2 [e.g., Giehl et al., 2013, Moussallam et al., 2013, Toplis and Carroll, 1995].

3.3. *Capsule preparation*

We used Au gold capsules (1.5 cm long, 2.5 mm inner diameter, 0.2 mm wall thickness) since this metal minimizes the Fe-loss towards the capsule walls under reducing conditions. Distilled H_2O was first loaded, then silver oxalate as the source of CO_2 for H_2O-undersaturated runs, and then the glass powder. Capsules were weighed and then welded using an arc-electric welder. After welding, capsules were re-weighed and if no significant weight loss occurred (considered to occur for a difference >0.0004 g (or ≤0.1% of the final weight of the capsule)), they were left in an oven for a few hours at 100 °C, to ensure homogeneous volatiles distribution. Both the amount of H_2O+CO_2 and fluid/silicate ratio were maintained constant (3 ± 0.5 mg of H_2O+CO_2, and 30 mg silicate). At a given T–P conditions, various starting

H_2O–CO_2 mixtures were explored: XH_2O_{in}, defined as $H_2O/(H_2O + CO_2)$ (in moles), varied in the range 1–0.08 (Table 2).

A typical experiment contained five or six capsules, each loaded with a different H_2O/CO_2 ratio. Run duration varied between 64 and 74 h, depending on temperature. Experiments were terminated by using the drop quench device and then switching off the power supply. After the experiments, capsules were checked for leaks, opened, and half of the run product was embedded in a probe mount with an epoxy resin and polished for optical observation, and carbon coated for subsequent EMPA and scanning electron microscopy (SEM) characterisation.

3.4. *Water content, fH_2, fO_2 in the capsules*

The variation of the XH_2O_{in} in the capsules allowed us to explore different water fugacities, and thus different H_2O_{melt} (Table 2). The amount of dissolved water (XH_2O_{in}) in the glass of the different H_2O-saturated charges was calculated using the H_2O-solubility model of Jiménez-Mejías et al. [2021] which is suited for basanitic–phonotephritic compositions. The water contents of charges with $XH_2O_{in} < 1$ ran at the same temperature and pressure than the H_2O-saturated charge, were calculated by mass balance using the constraint of equilibrium fugacities of H_2O and CO_2 species between melt and fluid, along with the H_2O–CO_2 solubility model of Jiménez-Mejías et al. [2021].

The fH_2 of the experiments was determined using an empirical calibration curve established in previous experimental works, relating the H_2 pressure loaded initially to the autoclave at room temperature to the final fH_2 as determined using NiPd sensors run at similar P–T–fO_2 [Andújar and Scaillet, 2012, Andújar et al., 2015, Romano et al., 2018]. Once the prevailing fH_2 is known, the fO_2 can be determined by using the dissociation constant of water [Robie et al., 1979], knowing the fH_2O at the experimental temperature and pressure. fH_2O was calculated as $fH_2O = XH_2O_{in} * fH_2O^o$ where fH_2O^o is the fugacity of pure water [Burnham et al., 1969]. Afterwards, the fO_2 for each capsule was calculated (Table 2) (see Andújar and Scaillet [2012] for further details). The experiments were conducted at oxygen fugacities around NNO ± 0.3 at H_2O-saturation. As fO_2 decreases with XH_2O_{in} [e.g., Andújar and Scaillet, 2012, Freise et al., 2009, Scaillet et al., 1995, Webster et al., 1987], at fixed T, P, fH_2, for water-undersaturated charges the prevailing oxygen fugacity is necessarily <NNO ± 0.3. As a result, in a single experimental series, the decrease in XH_2O_{in} from 1 to 0.08 decreased the fO_2 up to about 2.5 log units below the NNO buffer (or ~1.8 log units below the Fayalite-Magnetite-Quarz buffer, FMQ; Table 2).

3.5. *Analytical techniques*

Experimental runs were first characterized using a Zeiss Merlin Compact electron microscope equipped with an EDS micro-analysis system (Bruker-Quantax-XFlash6) at ISTO. EDS spectra allowed a first order identification of the minerals present in each charge. Experimental phases were analyzed using a Cameca SX-Five EPMA with an acceleration voltage of 15 kV, a sample current of 6 nA, and a counting time of 10 s. For glasses, a defocused beam of 20 μm was used whereas for minerals a focused beam was employed instead. Sodium and potassium were analyzed first and a Phi-Rho-Z correction procedure was applied. Major elements calibration was done using the following standards: albite (Na, Si), orthoclase (K), andradite (Ca), apatite (P), chromite (Cr), corundum (Al), magnesium oxide (Mg), hematite (Fe) and pyrophanite (Mn, Ti). The relative analytical errors are 1% (SiO_2, Al_2O_3, CaO), 3% (FeO, MgO, TiO_2) and 5% (MnO, Na_2O, K_2O, P_2O_5).

In the case of experimental plagioclase (Pl), the small size of this phase in the charges (usually ≤3 μm) along with the presence of small (≤0.5 μm) Fe–Ti oxides-apatite inclusions inside the crystals, made difficult the proper analysis of this phase with EPMA. To circumvent this problem, Pl composition was obtained via using a SEM-EDS calibrated analysis: albite, orthose and andradite EMPA standards were analyzed first with a focused beam (1 μm), a voltage of 15 kV and counting times of 15 s for the different elements (Na, K, Si, Al, Ca, Na, K). SEM-EDS compositions of the standards were found to be within ≤5% to those obtained by EMPA (see Supplementary Table). Consequently, experimental plagioclases were determined by SEM-EDS in each charge, using the same conditions and the average SEM-EDS calibrated compositions fulfilling the stoichiometric requirements for this phase (see Supplementary Table).

Table 1. 100 wt% anhydrous composition of the starting glass DR08, dredge bulk-rock compositions for submarine basanite DR08 and phonolites [Berthod et al., 2021a,b]; North-central onland phonolites

DR08	DR08 Starting Glass	sd	Bulk-rock submarine basanite Berthod et al. [2021a,b]		Bulk-rock submarine phonolites					North central onland-phonolites [Pelleter et al., 2014, Späth et al., 1996]				
			DR0801-ALF	DR080102	DR020202	DR020401	DR060204	DR070201	DR0701	M29 (aphyric)	M31	M76	Ma-5	Ma65
n	15													
SiO_2	47.45	0.33	47.65	47.44	58.54	58.50	58.59	58.43	59.12	61.47	57.60	59.65	60.10	58.65
TiO_2	2.87	0.13	2.90	2.92	0.37	0.36	0.36	0.35	0.36	0.35	0.87	0.56	0.58	0.81
Al_2O_3	15.35	0.16	15.69	15.53	18.51	18.47	18.65	18.67	18.37	19.79	20.24	19.95	19.91	19.14
FeO*	13.61	0.35	13.74	14.00	6.47	6.44	6.50	6.68	6.48	3.15	4.75	4.01	3.77	5.12
MnO	0.19	0.04	0.24	0.25	0.26	0.26	0.27	0.27	0.27	0.12	0.14	0.13	0.14	0.17
MgO	4.57	0.10	4.43	4.46	0.62	0.63	0.46	0.40	0.47	0.49	1.02	0.46	0.45	0.79
CaO	6.61	0.06	6.53	6.53	1.57	1.55	1.63	1.62	1.65	1.45	3.16	2.26	1.97	3.03
Na_2O	4.79	0.06	4.48	4.62	7.97	8.05	7.64	7.67	7.48	7.38	7.36	7.66	8.07	7.67
K_2O	2.74	0.11	2.75	2.63	5.39	5.47	5.61	5.60	5.48	5.70	4.62	5.20	4.91	4.40
P_2O_5	1.81	0.05	1.58	1.60	0.31	0.28	0.31	0.31	0.32	0.09	0.25	0.11	0.08	0.22
Sum	100.00		100	100	100	100	100	100	100	100	100	100	100	100
P.I.	0.71		0.66	0.68	1.03	1.04	1.01	1.01	1.00	0.93	0.85	0.92	0.94	0.91
Normative Nepheline (wt%)					12.6	13.2	11.5	11.8	9.4	7.4	10.8	10.4	10.7	9.4

n: Number of analysis.

sd: Standard deviation.

P.I: Peralkaline index calculated as the (Na+K)/Al in moles.

Table 2. Experimental run conditions and phase proportions (wt%)

Charge	T (°C)	P	XH_2O_{in}	XH_2O_{fin}	H_2O (wt%)	CO_2 (ppm)	fH_2O	$\log fO_2$	ΔNNO	ΔQFM	Ol	Mt	Ilm	Ap	Cpx	Pl	Kr	Bt	Observations	% crystals	R2
950 °C/400 MPa; t = 73 h																					
DR08-140	950	400	1.00	1.00	6.78	0	3880	−10.7	0.3	0.87		7.7		3.8			12.4	5.2		29.1	0.61
DR08-141	950	400	0.72	0.52	4.78	4593	2015	−11.3	−0.3	0.30		6.15	0.1	3.3			25.8	2.5		37.85	0.42
DR08-142	950	400	0.49	0.27	3.40	5483	1062	−11.9	−0.8	−0.25	2.9	5.6	0.37	4.7			20.6	2.1		36.27	0.23
DR08-143	950	400	0.26	0.10	1.97	5974	381	−12.8	−1.7	−1.15	14.05	0.94	3.4	3.86		34.07	9	0.7		66.02	0.73
DR08-144	950	400	0.14	0.04	1.29	6108	172	−13.5	−2.4	−1.83	X	X	X	X		X	X	X			
DR08-145	950	400	0.09	0.03	0.96	6154	100	−13.9	−2.9	−2.31	X	X	X	X	X	X	X	X			
925 °C/400 MPa; t = 71.5 h																					
DR08-152	925	400	1.00	1.00	6.69	0	3779	−11.2	0.2	0.81		7.6	0.2	4.01			15.6	7.8		35.21	0.38
DR08-154	925	400	0.50	0.31	3.59	5402	1173	−12.2	−0.8	−0.21		5.6	0.51	3.5		14.4	25.7	7.8		57.51	0.75
DR08-155	925	400	0.29	0.16	2.51	5850	599	−12.8	−1.4	−0.79	X	X	X	X		X	X	X			
DR08-156	925	400	0.18	0.09	1.86	6030	340	−13.3	−1.9	−1.29	X	X	X	X		X	X	X			
DR08-157	925	400	0.08	0.03	1.09	6170	127	−14.2	−2.7	−2.14	X	X	X	X	X	X	X	X			
DR08-950 °C, 200 MPa, t = 68 h																					
DR08-56	950	200	0.90	0.85	4.65	249	1527	−11.6	−0.5	0.81	2.3	8.8		3.2			20	2.6		36.9	1.2
DR08-58	950	200	0.51	0.34	2.73	908	613	−12.3	−1.3	1.03	3.01	7.1		3.6			25	2.1		40.81	0.93
DR08-925 °C/200 MPa, 69.5 h																					
DR08-129	925	200	1.00	1.00	5.06	–	1764	−11.9	−0.4	0.14		7.1		3.97			26.5	2.3	Quench	39.87	0.96
DR08-130	925	200	0.88	0.82	4.52	287	1452	−12.1	−0.6	−0.02		5.7		2.4			30.5	3.8		42.4	0.99
DR08-131	925	200	0.69	0.60	3.76	596	1060	−12.3	−0.8	−0.30	15.9	1	3.8	4.3		31.29	8.2	0.4		64.89	0.67
DR08-132	925	200	0.45	0.35	2.73	900	614	−12.8	−1.3	−0.77	x	x	x	x	x	x	x	x			
DR08-133	925	200	0.34	0.25	2.27	1004	449	−13.1	−1.6	−1.04	x	x	x	x	x	x		x			
DR08-134	925	200	0.19	0.13	1.49	1138	226	−13.7	−2.2	−1.66	x	x	x	x	x	x		?			
DR08-135	925	200	0.09	0.05	0.84	1215	93	−14.4	−2.9	−2.45	x	x	x	x	x	x		?			

(continued on next page)

Table 2. (continued)

Charge	T (°C)	P	XH_2O_{in}	XH_2O_{fin}	H_2O (wt%)	CO_2 (ppm)	fH_2O	$\log fO_2$	ΔNNO	ΔQFM	Ol	Mt	Ilm	Ap	Cpx	Pl	Kr	Bt	Observations	% crystals	R2
DR08-925 °C/150 MPa; t = 71, 5h																					
DR08-158	925	150	1.00	1.00	3.85	0	1339	−11.8	−0.3	0.26		7.72		4.01			20.6	4.8		37.13	0.32
DR08-159	925	150	0.90	0.86	3.56	259	1154	−11.9	−0.4	0.13		7.74		3.72		3.74	22.7	3.1		41	0.5
DR08-160	925	150	0.65	0.52	2.72	998	698	−12.3	−0.8	−0.31	7.44	7.76	1.73	3.59	2.3	12.8	18.4	0.9		54.92	0.33
DR08-161	925	150	0.54	0.45	2.52	1164	603	−12.5	−1.0	−0.44	X	X	X	X	X	X	X	X			
DR08-162	925	150	0.30	0.21	1.66	1719	277	−13.1	−1.6	−1.11	X	X	X	X	X	X		X			
DR08-163	925	150	0.18	0.12	1.26	1897	165	−13.6	−2.1	−1.58	X	X	X	X	X	X		X			
DR08-925 °C/100 MPa; t = 64 h																					
DR08-164	925	100	1.00	1.00	3.14	0	915	−11.8	−0.3	0.18	2.45	8.18		3.7		14.5	18.9	3.1		50.83	0.56
DR08-165	925	100	0.88	0.84	2.87	168	772	−12.0	−0.5	0.03	5.33	7.6	1.09	4.03	6.39	21.3	2.9	5.5		54.14	0.4
DR08-166	925	100	0.71	0.62	2.44	424	571	−12.3	−0.7	−0.23	X	X	X	X	X	X		X			
DR08-167	925	100	0.47	0.37	1.86	741	341	−12.7	−1.2	−0.68	X	X	X	X	X	X		X			
DR08-168	925	100	0.33	0.24	1.46	921	217	−13.1	−1.6	−1.07	X	X	X	X	X	X		X			

Ol: olvine, Mt: magnetite, ilm: ilmenite, Ap: apatite, Cpx: Clinopyroxene, Pl: plagioclase, Kr: Kaersutite/Amphibole, Bt: biotite.

XH_2O_{in} =, initial $H_2O/(H_2O+CO_2)$ in the charge.

XH_2O_{fin} = final $H_2O/(H_2O+CO_2)$ in the charge.

H_2O wt%, water content in the melt in wt%.

CO_2 content in the melt ppm.

$\log fO_2$(bar), logarithm of the oxygen fugacity calculated from the experimental fH_2.

ΔNNO = $\log fO_2$ experiment-$\log fO_2$ of the NNO buffer calculated at experimental T–P after Pownceby and O'Neill [1994].

ΔQFM = $\log fO_2$ experiment-$\log fO_2$ of the QFM buffer calculated at experimental T after Chou [1978].

X, mineral phase identified by SEM but, its abundance could not be calculated.

fH_2(bar), hydrogen fugacity of the experiment. See text for details.

Table 3. Experimental olivine compositions (wt%)

Charge	T (°C)	P (MPa)	n	SiO_2	TiO_2	Al_2O_3	FeO*	MnO	MgO	CaO	Na_2O	K_2O	Sum	Fo%
DR08-142	950	400	3	33.5	0.2	0.2	43.8	1.1	19.9	0.7	0.1	0.0	99.5	44.8
sd				0.4	0.1	0.2	1.0	0.1	0.3	0.4	0.1	0.0	0.7	0.2
DR08-143	950	400	2	32.9	0.3	0.1	47.3	1.2	17.6	0.9	0.1	0.0	100.5	39.9
sd				0.0	0.0	0.0	0.2	0.1	0.2	0.1	0.0	0.0	0.0	0.3
DR08-144	950	400	1	32.8	0.5	0.7	48.9	1.3	16.4	0.8	0.1	0.1	101.7	37.5
DR08-145	950	400	1	34.2	0.3	1.5	45.0	1.6	15.0	1.1	0.3	0.2	99.2	37.3
DR08-155	925	400	2	32.7	0.2	0.1	50.3	1.8	13.9	1.3	0.1	0.1	100.5	33.0
sd				0.5	0.1	0.1	1.0	0.1	0.5	0.2	0.0	0.1	0.7	0.4
DR08-157	925	400	1	32.7	0.5	0.5	49.3	1.4	13.5	1.6	0.1	0.1	99.6	32.8
DR08-58	950	200	2	33.3	0.3	0.1	40.2	1.2	21.6	1.2	0.0	0.0	97.9	49.0
sd				0.4	0.3	0.1	0.3	0.1	0.6	0.5	0.0	0.0	0.2	0.9
DR08-131	925	200	1	33.5	0.2	0.5	42.6	1.7	19.2	1.0	0.2	0.1	98.9	44.5
DR08-132	925	200	2	32.1	0.8	0.6	42.4	1.5	18.6	1.3	0.2	0.1	97.5	43.9
sd				1.0	0.5	0.3	1.1	0.1	0.5	0.2	0.0	0.0	1.2	0.5
DR08-160	925	150	1	34.8	0.1	0.0	40.6	1.4	22.4	0.5	0.0	0.0	99.8	49.6
DR08-161	925	150	2	34.8	0.1	0.6	40.6	1.7	22.2	0.4	0.3	0.1	100.8	49.4
sd				0.1	0.1	0.1	0.5	0.3	0.3	0.1	0.0	0.0	0.8	0.6
DR08-162	925	150	1	31.6	1.3	0.5	44.0	1.3	18.6	1.7	0.1	0.1	99.3	42.9
DR08-164	925	100	2	34.3	0.1	0.4	38.8	1.4	22.8	1.8	0.1	0.0	99.8	51.1
sd				0.7	0.1	0.1	0.2	0.0	0.0	0.4	0.1	0.0	0.3	0.1
DR08-165	925	100	1	32.1	1.0	0.2	40.4	1.3	22.0	1.6	0.0	0.1	98.7	49.2
DR08-166	925	100	2	32.7	1.0	0.8	40.1	1.3	20.9	2.0	0.2	0.1	99.2	48.2
sd				0.6	0.4	0.2	0.3	0.1	0.3	0.2	0.1	0.0	0.5	0.1

n: number of analysis.

sd: standard deviation.

FeO*: Total iron reported as Fe^{2+}.

Fo mole(%) = 100 Mg/(Mg + Fe*) in olivine.

It should be noted that, compared to EMPA analyses, which are characterized by lower standard deviations (see Tables 3–8), SEM-EDS compositions are slightly more variable (see Supplementary Table), with a variation of ~2–3 mol% on end-member molecules. However, despite this, we can still use these compositions for comparison purposes.

3.6. *Attainment of equilibrium*

The crystallization experiments performed in this work share similar phase stabilities, textural and compositional characteristics to those found in equivalent studies performed on alkali-rich basalts [e.g., Andújar et al., 2015, Freise et al., 2009, Iacovino et al., 2016] using a similar procedure. As in these works, the following observations show that near-equilibrium conditions were attained in our experiments: the euhedral shape of crystals, the homogeneous distribution of phases within the charges, the smooth variation of phase proportions and compositions with changes in experimental conditions, and the small sum of residuals of mass-balance (generally ≤1; Table 2). Since each experimental charge is a

Table 4. Experimental amphibole compositions (wt%). Classification after Ridolfi [2021]

Charge	T (°C)	P (MPa)	n	SiO_2	TiO_2	Al_2O_3	FeO*	MnO	MgO	CaO	Na_2O	K_2O	Sum	Species	Si	AlIV	Ti	T sum	AlVI	Ti	Cr	Fe^{3+}	Mg	Fe^{2+}	Mn	C sum	Ca	Na	B sum	Na	K	A sum	OH	F	Cl	W sum	Charge	Mg/(Mg + Fe^{2+})	Mg#	Al#	AlT
DR08-140	950	400	5	39.85	2.91	11.07	13.14	0.25	11.23	9.97	2.71	0.87	92.41	Mg-hastingsite	6.24	1.76	0.00	8.00	0.28	0.34	0.00	0.45	2.62	1.27	0.03	5.00	1.67	0.33	2.00	0.49	0.17	0.67	2.00	0.00	0.00	2.00	45.55	0.67	0.60	0.14	2.04
sd				0.53	0.23	0.35	1.00	0.07	0.76	0.08	0.05	0.10	0.89																												
DR08-141	950	400	2	39.16	3.72	12.10	16.20	0.28	9.97	11.72	2.75	0.91	96.83	Pargasite	6.00	2.00	0.00	8.00	0.18	0.43	0.00	0.12	2.28	1.95	0.04	5.00	1.92	0.08	2.00	0.74	0.18	0.92	2.00	0.00	0.00	2.00	45.88	0.54	0.52	0.08	2.18
sd				0.73	0.60	1.09	1.07	0.14	0.68	1.81	0.00	0.09	1.25																												
DR08-142	950	400	3	39.41	5.14	12.22	14.83	0.19	11.01	10.51	2.68	0.95	96.94	kaersutite	5.91	2.09	0.00	8.00	0.07	0.58	0.00	0.52	2.46	1.34	0.02	5.00	1.69	0.31	2.00	0.47	0.18	0.65	2.00	0.00	0.00	2.00	45.48	0.65	0.57	0.03	2.16
sd				0.97	0.35	0.57	0.58	0.06	0.39	0.36	0.20	0.12	0.68																												
DR08-143	950	400	3	38.60	5.55	11.77	16.27	0.36	9.23	11.83	2.71	1.12	97.44	kaersutite	5.95	2.05	0.00	8.00	0.09	0.64	0.00	0.00	2.12	2.10	0.05	5.00	1.95	0.05	2.00	0.76	0.22	0.98	2.00	0.00	0.00	2.00	46.27	0.50	0.50	0.04	2.14
sd				0.79	0.55	0.57	1.03	0.10	0.18	0.78	0.10	0.06	0.66																												
DR08-144	950	400	2	41.10	5.05	10.50	18.19	0.25	9.07	10.80	2.96	1.14	99.04	low-Mg	6.20	1.80	0.00	8.00	0.06	0.57	0.00	0.02	2.04	2.27	0.03	5.00	1.74	0.26	2.00	0.61	0.22	0.83	2.00	0.00	0.00	2.00	45.98	0.47	0.47	0.03	1.87
sd				0.11	0.03	0.28	0.89	0.05	0.26	0.48	0.03	0.09	1.54																												
DR08-145	950	400																																							
DR08-152	925	400	3	40.44	3.07	11.78	13.30	0.31	12.71	11.49	2.66	0.86	96.63	Mg-hastingsite	6.04	1.96	0.00	8.00	0.12	0.35	0.00	0.53	2.83	1.14	0.04	5.00	1.84	0.16	2.00	0.61	0.16	0.78	2.00	0.00	0.00	2.00	45.47	0.71	0.63	0.06	2.08
sd				0.57	0.19	0.70	0.40	0.06	0.50	0.21	0.10	0.08	0.92																												
DR08-154	925	400	4	40.25	3.79	11.11	18.85	0.42	9.00	10.41	2.98	0.68	97.48	Mg-hastingsite	6.10	1.90	0.00	8.00	0.09	0.43	0.00	0.56	2.04	1.83	0.05	5.00	1.69	0.31	2.00	0.57	0.13	0.70	2.00	0.00	0.00	2.00	45.44	0.53	0.46	0.04	1.99
sd				0.94	0.15	0.19	0.51	0.12	0.30	0.23	0.10	0.04	0.89																												
DR08-155	925	400	6	39.33	4.04	10.40	19.05	0.45	8.12	10.80	3.01	0.85	96.06	low-Mg	6.16	1.84	0.00	8.00	0.08	0.48	0.00	0.11	1.90	2.38	0.06	5.00	1.81	0.19	2.00	0.73	0.17	0.89	2.00	0.00	0.00	2.00	45.89	0.44	0.43	0.04	1.92
sd				0.61	0.20	0.23	0.40	0.05	0.20	0.26	0.07	0.03	0.47																												
DR08-156	925	400	1	39.48	4.32	10.75	18.24	0.45	7.66	11.42	2.98	0.92	96.23	low-Mg	6.22	1.78	0.00	8.00	0.22	0.51	0.00	0.00	1.80	2.41	0.06	5.00	1.93	0.07	2.00	0.84	0.18	1.02	2.00	0.00	0.00	2.00	46.42	0.43	0.43	0.11	2.00
DR08-157	925	400	1	40.53	3.89	12.15	17.63	0.32	7.00	10.99	3.23	0.96	96.70	low-Mg	6.33	1.67	0.00	8.00	0.57	0.46	0.00	0.00	1.63	2.30	0.04	5.00	1.84	0.16	2.00	0.82	0.19	1.01	2.00	0.00	0.00	2.00	46.66	0.41	0.41	0.25	2.24
sd																																									
DR08-56	950	200	5	39.495	4.4431	11.74	12.44	0.27	12.61	11.03	2.62	0.85	95.50	kaersutite	5.96	2.04	0.00	8.00	0.05	0.50	0.00	0.48	2.84	1.09	0.03	5.00	1.78	0.22	2.00	0.55	0.16	0.71	2.00	0.00	0.00	2.00	45.52	0.72	0.64	0.03	2.09
sd				0.2655	0.2434	0.22	0.11	0.05	0.15	0.23	0.13	0.08	0.44																												
DR08-58	950	200	5	39.336	5.0109	11.10	14.51	0.28	10.84	11.56	2.68	0.98	96.30	kaersutite	6.04	1.96	0.00	8.00	0.04	0.58	0.00	0.00	2.48	1.86	0.04	5.00	1.90	0.10	2.00	0.70	0.19	0.89	2.00	0.00	0.00	2.00	46.03	0.57	0.57	0.02	2.01
sd				0.1415	0.3008	0.36	0.69	0.07	0.08	0.53	0.12	0.10	0.88																												

(continued on next page)

Table 4. (continued)

Charge	T (°C)	P (MPa)	n	SiO_2	TiO_2	Al_2O_3	FeO*	MnO	MgO	CaO	Na_2O	K_2O	Sum	Species	Si	AlIV	Ti	T sum	AlVI	Ti	Cr	Fe^{3+}	Mg	Fe^{2+}	Mn	C sum	Ca	Na	B sum	Na	K	A sum	OH	F	Cl	W sum	Charge	Mg/(Mg + Fe^{2+})	Mg#	Al#	AlT
DR08-129	925	200	3	38.76	3.58	12.34	13.13	0.32	11.82	11.33	2.65	0.86	94.78	Mg-hastingsite	5.94	2.06	0.00	8.00	0.17	0.41	0.00	0.40	2.70	1.29	0.04	5.00	1.86	0.14	2.00	0.65	0.17	0.82	2.00	0.00	0.00	2.00	45.60	0.68	0.62	0.07	2.23
sd				0.12	0.16	0.08	0.08	0.07	0.28	0.26	0.07	0.16	0.17																												
DR08-131	925	200	3	39.08	3.78	11.19	16.27	0.33	10.49	10.75	2.83	0.84	95.57	Mg-hastingsite	6.00	2.00	0.00	8.00	0.03	0.44	0.00	0.55	2.40	1.54	0.04	5.00	1.77	0.23	2.00	0.61	0.16	0.78	2.00	0.00	0.00	2.00	45.45	0.61	0.53	0.01	2.03
sd				0.05	0.08	0.00	0.31	0.03	0.21	0.10	0.13	0.02	0.14																												
DR08-158	925	150	3	40.12	3.67	11.78	15.39	0.26	11.38	11.22	2.82	0.68	97.34	Mg-hastingsite	6.01	1.99	0.00	8.00	0.09	0.41	0.00	0.53	2.54	1.40	0.03	5.00	1.80	0.20	2.00	0.62	0.13	0.75	2.00	0.00	0.00	2.00	45.47	0.65	0.57	0.04	2.08
sd				0.83	0.23	0.25	0.30	0.10	0.28	0.23	0.02	0.15	0.84																												
DR08-159	925	150	3	40.63	3.68	11.43	15.42	0.36	11.21	11.07	2.89	0.69	97.38	Mg-hastingsite	6.09	1.91	0.00	8.00	0.10	0.41	0.00	0.45	2.50	1.48	0.05	5.00	1.78	0.22	2.00	0.62	0.13	0.75	2.00	0.00	0.00	2.00	45.55	0.63	0.56	0.05	2.02
sd				0.16	0.14	0.06	0.55	0.13	0.11	0.30	0.10	0.09	0.29																												
DR08-160	925	150	3	39.45	3.93	10.65	15.66	0.37	10.56	11.71	3.01	0.86	96.19	Pargasite	6.10	1.90	0.00	8.00	0.04	0.46	0.00	0.00	2.43	2.02	0.05	5.00	1.94	0.06	2.00	0.84	0.17	1.01	2.00	0.00	0.00	2.00	46.00	0.55	0.55	0.02	1.94
sd				0.38	0.11	0.38	0.43	0.09	0.43	0.62	0.04	0.10	0.76																												
DR08-161	925	150	1	40.30	4.19	10.89	16.32	0.44	10.64	11.03	2.89	0.85	97.56	Mg-hastingsite	6.08	1.92	0.00	8.00	0.02	0.48	0.00	0.38	2.39	1.68	0.06	5.00	1.78	0.22	2.00	0.63	0.16	0.79	2.00	0.00	0.00	2.00	45.62	0.59	0.54	0.01	1.94
DR08-164	925	100	4	39.99	4.23	11.07	14.57	0.28	11.14	11.70	2.81	0.71	96.51	Pargasite	6.10	1.90	0.00	8.00	0.09	0.49	0.00	0.05	2.53	1.81	0.04	5.00	1.91	0.09	2.00	0.74	0.14	0.88	2.00	0.00	0.00	2.00	45.95	0.58	0.58	0.04	1.99
sd				0.18	0.25	0.16	0.24	0.10	0.14	0.25	0.10	0.05	0.29																												
DR08-165	925	100	2	39.74	4.36	10.53	14.83	0.34	10.85	12.21	2.91	0.83	96.60	kaersutite	6.13	1.87	0.00	8.00	0.04	0.51	0.00	0.00	2.49	1.91	0.04	5.00	2.02	-0.02	2.00	0.89	0.16	1.05	2.00	0.00	0.00	2.00	46.25	0.57	0.57	0.02	1.91
sd				0.54	0.16	0.34	0.12	0.05	0.09	0.59	0.07	0.00	0.68																												
DR08-166	925	100	2	39.54	4.46	10.17	14.92	0.25	10.59	12.29	2.88	0.93	96.04	kaersutite	6.17	1.83	0.00	8.00	0.04	0.52	0.00	0.00	2.46	1.95	0.03	5.00	2.05	-0.05	2.00	0.93	0.19	1.11	2.00	0.00	0.00	2.00	46.41	0.56	0.56	0.02	1.87
sd				0.27	0.12	0.68	0.05	0.12	0.21	0.72	0.01	0.04	0.79																												

n: number of analysis.

sd: standard deviation.

FeO*: Total iron reported as Fe^{2+}.

Table 5. Experimental biotite composition

Charge	T (°C)	P (MPa)	n	SiO_2	TiO_2	Al_2O_3	FeO*	MnO	MgO	CaO	Na_2O	K_2O	Sum	Mg#
DR08-140	950	400	2	35.02	3.67	14.25	11.51	0.10	15.30	0.10	1.40	7.19	88.55	70.33
sd				0.83	0.02	0.38	0.06	0.04	0.68	0.08	0.13	0.08	0.24	
DR08-141	950	400	1	34.77	5.54	15.35	16.50	0.09	12.35	0.11	1.27	7.17	93.15	57.16
DR08-145	950	400	1	38.21	7.24	14.21	17.26	0.13	8.51	3.04	1.63	6.46	96.70	46.78
DR08-152	925	400	1	37.27	3.96	15.79	16.29	0.18	12.79	0.37	1.50	7.14	95.28	58.32
DR08-130	925	200	1	34.77	5.81	15.40	18.24	0.11	12.23	0.55	1.24	7.18	95.53	54.44
DR08-158	925	150	1	37.86	4.87	16.12	15.23	0.15	11.85	0.51	1.43	6.50	94.51	58.11
DR08-159	925	150	1	34.11	5.56	14.27	16.37	0.26	13.18	0.27	1.34	6.73	92.08	58.93

n: number of analysis.

sd: standard deviation.

FeO*: Total iron reported as Fe^{2+}.

Mg# = 100*(MgO/MgO + FeO*).

closed-system, the low-residuals indicate that there was no mass loss or gain during the experiments, and that no major mineral phase has been omitted in our calculations.

4. Results

Phase proportions were obtained by mass-balance calculations of the charges using the bulk rock composition and the composition of the different mineral and glass phases. Results are provided in Table 2.

4.1. *Phase relationships*

The main mineral phases crystallizing in our runs are Bt (biotite), Amp (Kaersutite-type), Ol, Mt, Ilm, Ap, Pl and Cpx, with different glass proportions. Variations in temperature, pressure and H_2O_{melt} directly affect the stability and relationships of the different minerals. These changes are displayed in two isothermal-polybaric sections described below (Figure 3).

At 925 °C, the water-rich part of the diagram (H_2O_{melt} > 4 wt%) is dominated by the assemblage Bt+Amp+Mt+Ap+melt, followed by Ilm, Pl and Cpx with decreasing H_2O_{melt} (Figure 3A). Cpx coexists in a relatively narrow H_2O_{melt} region with Amp, both being involved along with Pl and melt, in a reaction-relationship that results in the disappearance of Amp at lower H_2O_{melt} (Figure 3A). Bt is stable everywhere in the P–H_2O_{melt} space explored. However, the decrease of its modal proportion with H_2O_{melt} (Table 2) and the consequent enrichment of the residual liquid in K_2O point towards its instability in the driest part of the system (Figure 3A). Hence, at 925 °C and for H_2O_{melt} < 1 wt%, the mineral assemblage that dominates the explored P-H_2O_{melt} region is Ol+Cpx+Pl+Ap+Mt+Ilm.

At this temperature and for pressures between 100 and 200 MPa, the Amp-out and Cpx, Ol, Ilm and Pl-in curves display steep or even vertical slopes, all occurring in a narrow H_2O_{melt} interval between 2.5–3 wt% (Figure 3A). Above 200 MPa, Cpx-in and Amp-out curves shrink towards lower H_2O_{melt} (≤2 wt%) whereas Ilm stability shifts towards higher H_2O_{melt}. Pressure does not have any major effect on Ol and Pl saturation curves.

At 950 °C, the general topology is broadly similar to that at 925 °C (Figure 3B), with Pl and Cpx appearing at H_2O_{melt} < 2–3 wt%, as anticipated, and Ol crystallizing first relative to Pl.

4.2. *Phase proportions*

Since experiments were performed at relatively low temperatures, liquidus conditions were not reached during the experiments. Charges always contained different amounts of crystals, which vary between 29 and 66 wt% (Figure 4A). In general, at fixed P–T conditions, the crystal proportions increase as H_2O_{melt} decreases (Figure 4A). Amp is the dominant phase

Table 6. Experimental Magnetite and ilmenite compositions (wt%)

Charge	T (°C)	P (MPa)	n	SiO_2	TiO_2	Al_2O_3	FeO*	MnO	MgO	CaO	Na_2O	K_2O	Cr_2O_3	Sum	X-Usp	X-Ilm
DR08-140	950	400	1	0.17	20.16	3.45	72.00	0.70	2.70	0.19	0.06	0.10	0.46	100	0.60	
DR08-141	950	400	1	1.80	49.68	1.82	41.63	0.78	2.26	1.41	0.33	0.21	0.09	100		0.99
DR08-141	950	400	1	0.11	21.47	4.31	71.25	0.64	2.00	0.08	0.05	0.07	0.03	100	0.67	
DR08-142	950	400	1	0.10	50.89	0.38	44.61	1.07	2.50	0.29	0.04	0.09	0.03	100		0.95
DR08-142	950	400	1	0.12	21.43	4.59	71.06	0.66	1.92	0.15	0.03	0.01	0.04	100	0.67	
DR08-143	950	400	1	0.10	21.79	4.22	71.05	0.66	1.93	0.10	0.04	0.05	0.05	100	0.68	
DR08-152	925	400	1	0.11	49.52	0.20	46.08	0.96	2.82	0.20	0.04	0.05	0.02	100		0.92
DR08-152	925	400	1	0.03	19.91	3.07	73.05	0.95	1.94	0.11	0.06	0.07	0.81	100	0.59	
DR08-154	925	400	1	0.72	21.63	3.02	70.50	1.11	1.53	0.29	0.03	0.12	1.04	100	0.67	
DR08-56	950	200	3	0.37	21.93	3.66	69.75	0.78	2.94	0.28	0.03	0.06	0.14	100	0.66	
sd				0.18	0.33	0.05	0.98	0.05	0.03	0.05	0.02	0.04	0.03			
DR08-58	950	200	1	0.33	24.63	3.20	67.79	0.78	2.74	0.33	0.00	0.15	0.00	100	0.74	
DR08-129	925	200	1	0.46	20.15	3.45	71.65	0.92	2.41	0.31	0.04	0.07	0.53	100	0.61	
DR08-131	925	200	1	0.32	20.06	3.88	70.74	0.96	2.14	0.26	0.00	0.07	1.58	100	0.62	
DR08-158	925	150	1	0.71	18.75	3.57	72.26	0.79	2.37	0.92	0.07	0.03	0.53	100	0.57	
DR08-159	925	150	1	0.44	18.16	3.61	73.69	0.87	2.34	0.76	0.00	0.08	0.04	100	0.54	
DR08-160	925	150	1	0.28	20.01	2.82	72.36	0.94	2.27	0.23	0.00	0.02	1.06	100	0.59	
DR08-161	925	150	1	0.11	21.76	2.27	70.29	1.13	2.21	0.20	0.04	0.07	1.91	100	0.63	
DR08-165	925	100	1	1.89	18.78	3.22	69.89	0.98	2.41	0.34	0.20	0.15	2.14	100	0.61	
DR08-165	925	100	1	0.06	51.45	0.18	41.95	1.57	4.58	0.18	0.00	0.02	0.02	100		0.94
DR08-166	925	100	1	1.67	19.18	2.92	70.17	0.94	2.14	0.38	0.17	0.14	2.29	100	0.61	
DR08-166	925	100	1	0.17	50.35	0.18	43.95	1.47	3.50	0.26	0.05	0.07	0.00	100		0.93

n: number of analysis.

sd: standard deviation.

FeO*: Total iron reported as Fe^{2+}.

X-Ilm: Ilmenite fraction in in ilmenite calculated as in Andersen and Lindsley [1998].

X-Usp: Ulvöspinel fraction in Magnetite calculated as in Andersen and Lindsley [1998].

Table 7. Experimental clinopyroxenes composition (wt%)

Charge	T (°C)	P (MPa)	n	SiO_2	TiO_2	Al_2O_3	FeO*	MnO	MgO	CaO	Na_2O	K_2O	Total	En	Fs	Wo	Mg#
DR08-145	950	400	1	47.78	1.45	4.03	10.89	0.29	10.73	20.54	0.95	0.37	97.03	33.77	19.23	46.47	63.72
DR08-160	925	150	3	49.09	0.95	2.96	11.78	0.62	11.71	20.76	0.72	0.08	98.65	34.86	19.67	44.43	63.94
				0.60	0.19	0.16	0.57	0.09	0.13	0.19	0.09	0.04	0.66	0.15	0.70	0.82	0.85

n: number of analysis.

sd: standard deviation.

FeO*: Total iron reported as Fe^{2+}.

Table 8. Composition of experimental glasses normalized to 100% anhydrous (wt%)

Charge	T (°C)	P (MPa)	n	SiO_2	TiO_2	Al_2O_3	FeO*	MnO	MgO	CaO	Na_2O	K_2O	P_2O_5	Total	Original sum	P.I. = (Na + K/Al)	Normative Nepheline (wt%)
DR08-140	950	400	5	58.57	0.99	18.37	6.83	0.17	1.61	4.33	5.98	2.75	0.39	100	85.72	0.70	
sd				0.42	0.08	0.25	0.22	0.07	0.08	0.07	0.56	0.15	0.07		0.53		
DR08-141	950	400	7	59.95	0.68	19.60	5.71	0.15	1.00	2.90	6.35	3.24	0.43	100	93.86	0.72	
sd				0.58	0.08	0.10	0.25	0.08	0.03	0.03	0.34	0.10	0.08		0.78		
DR08-142	950	400	3	60.50	0.68	19.97	6.13	0.15	1.00	2.90	6.53	3.24	0.19	100	95.13	0.72	
sd				0.61	0.18	0.18	0.21	0.06	0.20	0.04	0.29	0.07	0.01		0.83		
DR08-143	950	400	1	60.68	0.51	18.36	4.79	0.15	0.58	1.77	7.60	5.24	0.32	100	88.50	1.00	7.2
sd																	
DR08-152	925	400	3	60.41	0.78	18.98	5.66	0.15	0.97	3.71	6.34	2.59	0.42	100	88.08	0.70	
sd				0.34	0.13	0.23	0.46	0.11	0.16	0.06	0.18	0.05	0.20		0.36		
DR08-154	925	400	1	62.53	0.42	18.20	5.15	0.03	0.51	1.83	7.40	3.54	0.39	100	95.23	0.88	
DR08-56	950	200	2	58.01	0.95	18.59	7.08	0.29	1.50	3.87	6.25	3.19	0.30	100	92.90	0.74	
sd				0.44	0.09	0.09	0.21	0.01	0.07	0.01	0.16	0.03	0.02		0.93		
DR08-58	950	200	2	58.58	0.77	18.50	7.41	0.22	0.86	2.57	6.45	4.22	0.41	100	94.58	0.83	0.1
sd				0.53	0.05	0.07	0.37	0.11	0.00	0.07	0.08	0.09	0.15		0.28		
DR08-129	925	200	2	58.84	0.62	18.71	6.96	0.18	0.73	3.47	6.40	3.16	0.91	100	94.39	0.75	
sd				0.09	0.04	0.01	0.59	0.01	0.07	0.15	0.06	0.23	0.09		0.34		
DR08-130	925	200	2	59.00	1.09	18.96	6.55	0.17	0.67	3.16	6.32	3.24	0.83	100	93.87	0.74	
sd				0.38	0.71	0.50	0.02	0.11	0.01	0.01	0.16	0.03	0.22		1.34		
DR08-131	925	200	1	59.23	0.49	18.39	7.16	0.05	0.49	1.76	7.30	4.96	0.16	100	97.57	0.95	6.4

(continued on next page)

Table 8. (continued)

Charge	T (°C)	P (MPa)	n	SiO_2	TiO_2	Al_2O_3	FeO*	MnO	MgO	CaO	Na_2O	K_2O	P_2O_5	Total	Original sum	P.I. = (Na + K/Al)	Normative Nepheline (wt%)
DR08-158	925	150	9	60.78	0.68	19.29	5.02	0.16	1.01	3.04	6.51	3.21	0.31	100	92.67	0.74	
sd				0.34	0.09	0.34	0.21	0.08	0.03	0.07	0.28	0.14	0.05		0.68		
DR08-159	925	150	9	60.81	0.74	19.18	4.82	0.18	0.92	2.78	6.77	3.47	0.33	100	93.44	0.78	
sd				0.56	0.07	0.25	0.56	0.05	0.10	0.14	0.20	0.10	0.08		0.47		
DR08-160	925	150	2	60.52	0.63	19.25	4.92	0.16	0.80	2.73	6.75	3.80	0.44	100	95.98	0.79	
sd				0.82	0.04	0.13	0.10	0.15	0.06	0.68	0.02	0.28	0.45		1.23		
DR08-164	925	100	3	61.71	0.53	18.63	5.00	0.11	0.73	2.28	6.71	3.99	0.31	100	95.89	0.83	
sd				0.03	0.03	0.23	0.15	0.04	0.05	0.11	0.17	0.18	0.07		0.94		
DR08-165	925	100	2	61.81	0.59	19.39	5.02	0.00	0.74	2.10	6.44	3.78	0.14	100	94.98	0.76	
sd				0.07	0.04	0.45	0.18	0.00	0.02	0.02	0.13	0.25	0.15		0.35		

n: number of analysis.

sd: standard deviation.

FeO*: Total iron reported as Fe^{2+}.

P.I: peralkaline index calculated as the (Na + K)/Al in moles.

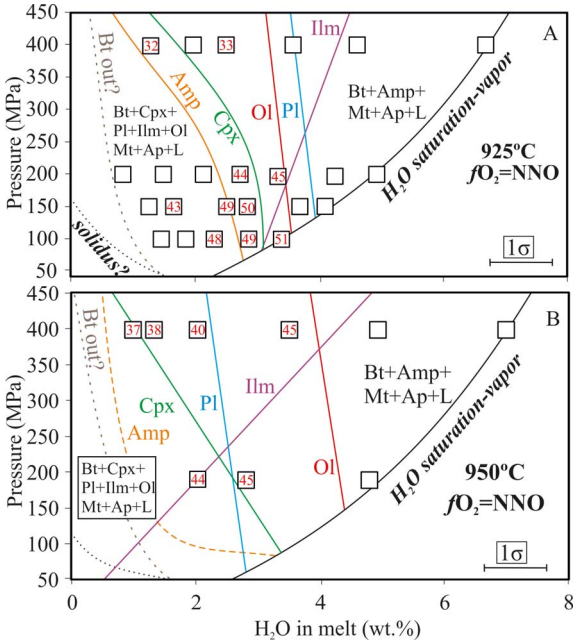

Figure 3. Isothermal phase relationships of the DR08 sample at (A) 925 °C and (B) 950 °C for different pressures and water contents in the melt. fO_2 ~ NNO: oxygen fugacity at water-saturation conditions. The decrease in XH_2O (hence H_2O_{melt}) results in a decrease in fO_2 in the capsules (see text for details). Mt: magnetite, Bt: biotite, Cpx: clinopyroxene, Ilm: ilmenite, Amp: amphibole, Pl: plagioclase, Ap: apatite; Ol: olivine, L: liquid. Dashed lines are estimated phase boundaries. Numbers inside squares indicate the forsterite content (Fo) in moles of the crystallizing olivines (see text for details).

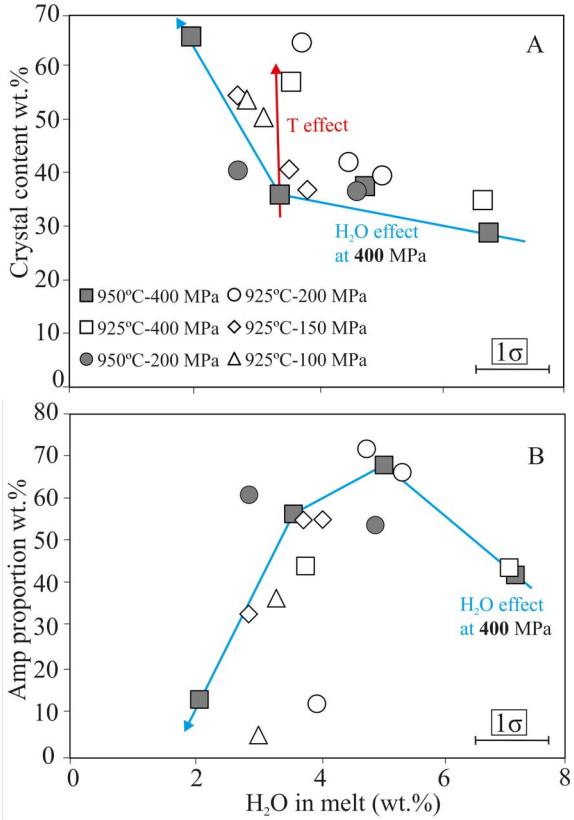

Figure 4. (A) Total crystal content of charges versus H_2O_{melt}. (B) Amph proportion in the fractionating crystal assemblage versus H_2O_{melt}. Vertical errors equal to symbol size.

whenever present, with proportions of up to 50–70 wt% of the crystallizing assemblage (Figure 4B); as H_2O_{melt} decreases, the Amp content decreases below 15 wt%. With decreasing H_2O_{melt}, Mt, Bt and Ap proportions steadily decrease while Ol, Ilm, Cpx and Pl increase. However, compared to Amp, any of these phases never exceed 15–25 wt% (Table 2).

4.3. *Phase compositions*

Experimental phase compositions (minerals and glass) are displayed in Tables 3–9, in supplementary and their variation with experimental variables (P–T and H_2O_{melt}) is discussed in the following sections.

4.3.1. *Olivine*

Ol crystallizing in our charges varies between Fo_{51-33}, with relatively constant contents of MnO (1.4 ± 0.2 wt%), depending on H_2O_{melt}, temperature and pressure conditions (Table 3). At a given P and T, a decrease in H_2O_{melt} decreases the Fo and increases the CaO content of Ol, similarly to the trends observed in other basaltic compositions [Andújar et al., 2015, 2017, Berndt et al., 2005, Di Carlo et al., 2006]. This is well exemplified at 400 MPa and 950 °C where a decrease in H_2O_{melt} of 2.5 wt% produces a diminution of 8 mol% of Fo (Figure 5A) and an increase of ~0.5 wt% in the CaO content of Ol (Figure 5B). A drop of 25 °C results in a relatively modest variation of Fo content, generally <5 mol% (Figure 5A). Series conducted at 925 °C allow to assess the effect of pressure on Ol composition. Considering a

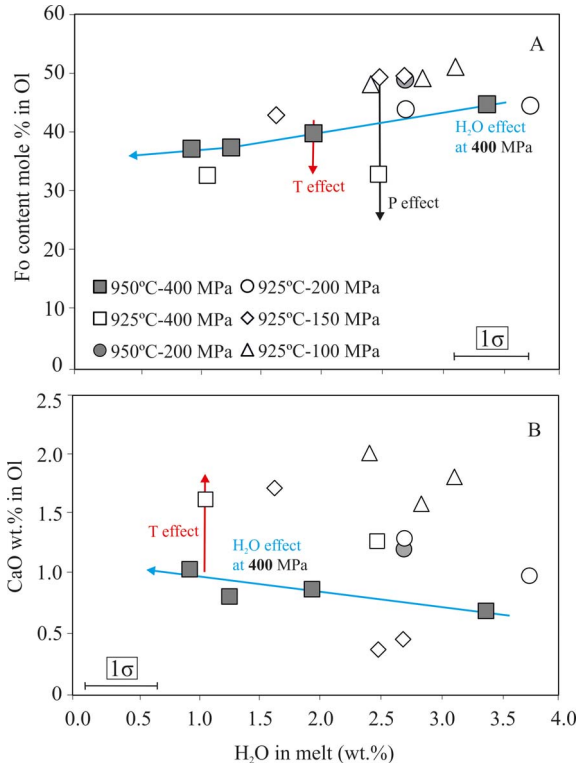

Figure 5. Composition of experimental olivine. (A) Fo content, (B) CaO (wt%) in Ol versus H_2O_{melt}. Vertical errors are equal to size symbols.

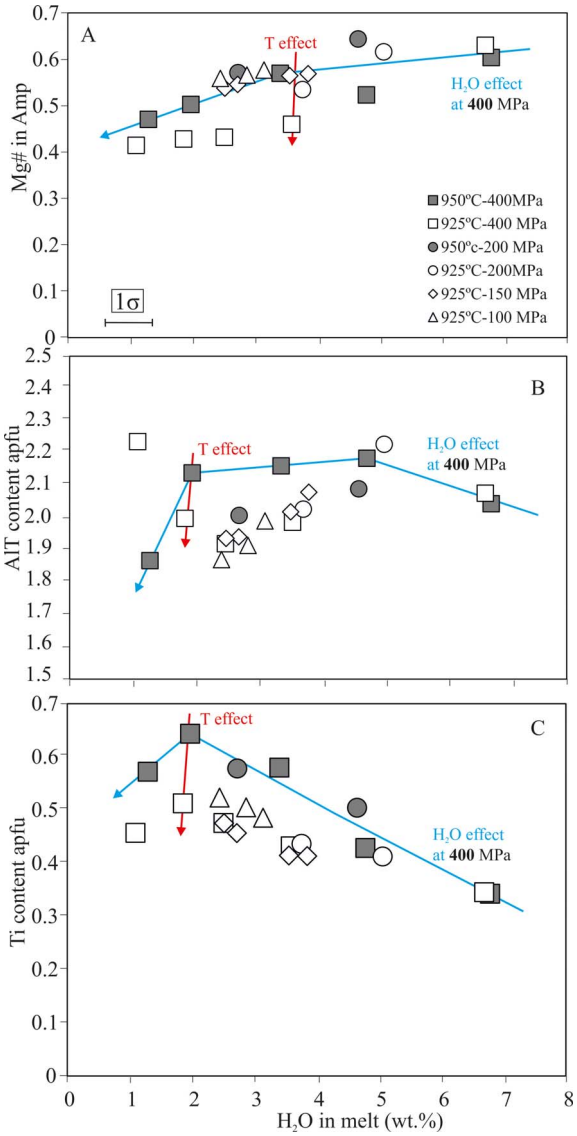

Figure 6. Composition of experimental amphibole. (A) Al total cations in atoms per formula unit (apfu), (B) Ti content and (C) Mg# = (Mg/Mg+Fe_{total}) versus H_2O_{melt}. Vertical errors equal to symbol size.

fixed H_2O_{melt} (e.g. 2.5–3 wt%), runs conducted between 100–150 MPa crystallized Ol with a similar composition (e.g. ~Fo_{50}). Increasing P by 50 MPa (so up to 200 MPa) produces changes in Ol composition that are equivalent to those observed with a T diminution (i.e., decrease of 8 mol% in Fo; Figure 5A). At higher pressures, the effect of this parameter in olivine composition is more pronounced, since at 400 MPa, crystallizing Ol are highly more fayalitic (Fo_{33}) compared to their shallower counterparts (e.g., Fo_{45-50} $P \leq 200$ MPa). The average Ol–liquid exchange (KdFe*–Mg; using FeO* as total iron) is 0.29 ± 0.1 (varying between 0.25 and 0.44).

4.3.2. *Amphibole*

Based on Ridolfi [2021], Amp that were synthetized in our runs vary between pargasite, Mg-hastingsite and kaersutite (Table 4). At a fixed P, amphibole Mg# (calculated with Fe* in atoms per formula unit, apfu), Al_{tot} and Al_{IV} decrease by ~20% relative (Figure 6A,B), while Ti increases, as H_2O_{melt} decreases (Figure 6C; Table 4). In series run at $P \leq 200$ MPa, a decrease of 25 °C does not significantly affect the composition of Amp. The variations of Al_{tot}, Al_{IV} and Al_{VI} with temperature and pressure have been widely used as a basis of empirical

thermometers and barometers to infer crystallization conditions of Amp-bearing magmas. In this work, however, neither Al_{IV} nor Al_{VI} show obvious correlations with pressure/temperature changes. Only Amp crystallized at 950 °C, 2–5 wt% H_2O_{melt} and 400 MPa have higher Al_{tot} contents (0.1–0.2 apfu) than their 200 MPa counterparts (Figure 6B).

4.3.3. *Biotite*

Representative analyses are presented in Table 5. The Mg# (calculated with FeO*) varies between 70 and 47 when H_2O_{melt} decreases from 7 to 1 wt%. TiO_2 content is inversely correlated with water content, the maximum (7 wt%) being achieved at ~1 wt% H_2O_{melt} and conditions of 950 °C–400 MPa. Water-saturated charges (DR08-140 and DR08-152) at 400 MPa show a difference of 10% in Mg# when *T* is decreased by 25 °C. Otherwise, under water-rich conditions and at constant *T* (e.g. 925 °C), the decompression of the system from 400 to 200 MPa produces Ti-rich biotites. The limited set of data does not allow us to provide further constraints on the effect of pressure or temperature on Bt composition.

4.3.4. *Fe–Ti oxides*

Mt has a relatively constant TiO_2 content at ~22 ± 2.5 wt%, with more variable FeO* (68–74 wt%). When present, Ilm was often too small to obtain reliable compositions by EPMA. Nevertheless, analyzed Ilm in 5 charges have almost constant TiO_2, at 50 wt%, and FeO* contents in the range 42–46 wt% (Tables 6–7). As for other phases, changes in experimental parameters affect Mt and Ilm compositions. The effect of H_2O_{melt} is significant: for example, in charges annealed at 950 °C–400 MPa, a decrease of 4 wt% H_2O_{melt} decreases Mg# by ~4% (Figure 7A), FeO* by 1.5 wt% and increases %Ulvöspinel from 60 to 70% (Figure 7B). The other experimental series display quite similar trends (Figure 7). A decrease in temperature of 25 °C produces similar changes. As for olivine, the effect of pressure on Mt composition is enhanced within the interval 200–400 MPa, low pressure Mt being enriched in Mg# and depleted in FeO* and %Ulvöspinel (compare series run at 950 °C–400 and 200 MPa in Figure 7).

4.3.5. *Plagioclase*

Pl are mostly andesines with compositions between An_{27}–An_{42} [Deer et al., 1972]. The most evolved Pl (oligoclase) crystallized instead in charges DR08-132, 155 and 161. As already observed in previous experimental studies performed on hydrous basaltic or basaltic andesite melts, Pl composition is highly sensitive to changes in H_2O_{melt} [e.g. Andújar et al., 2015, 2017]. The most important compositional variations are observed in charges run at 925 °C and $P \leq 150$ MPa, where the decrease in 2 wt% H_2O_{melt} results in a reduction of 10% in the mole fraction of An (see Supplementary Table). Similar variations in the CaO content of the experimental plagioclases can be produced when pressure decreases from 200 to 150 or 100 MPa at a given H_2O_{melt}, an effect that is again in agreement with the results of previous works [e.g. Andújar et al., 2015, 2017].

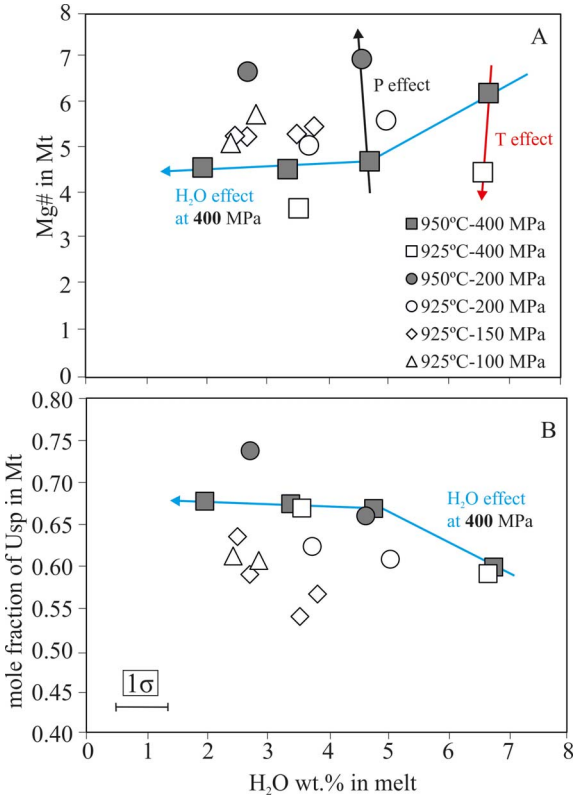

Figure 7. Composition of experimental magnetite. (A) Mg# = (MgO/MgO + FeO*), (B) Ulvöspinel content [calculated as in Andersen and Lindsley, 1998] versus H_2O_{melt}. Vertical errors equal to symbol size.

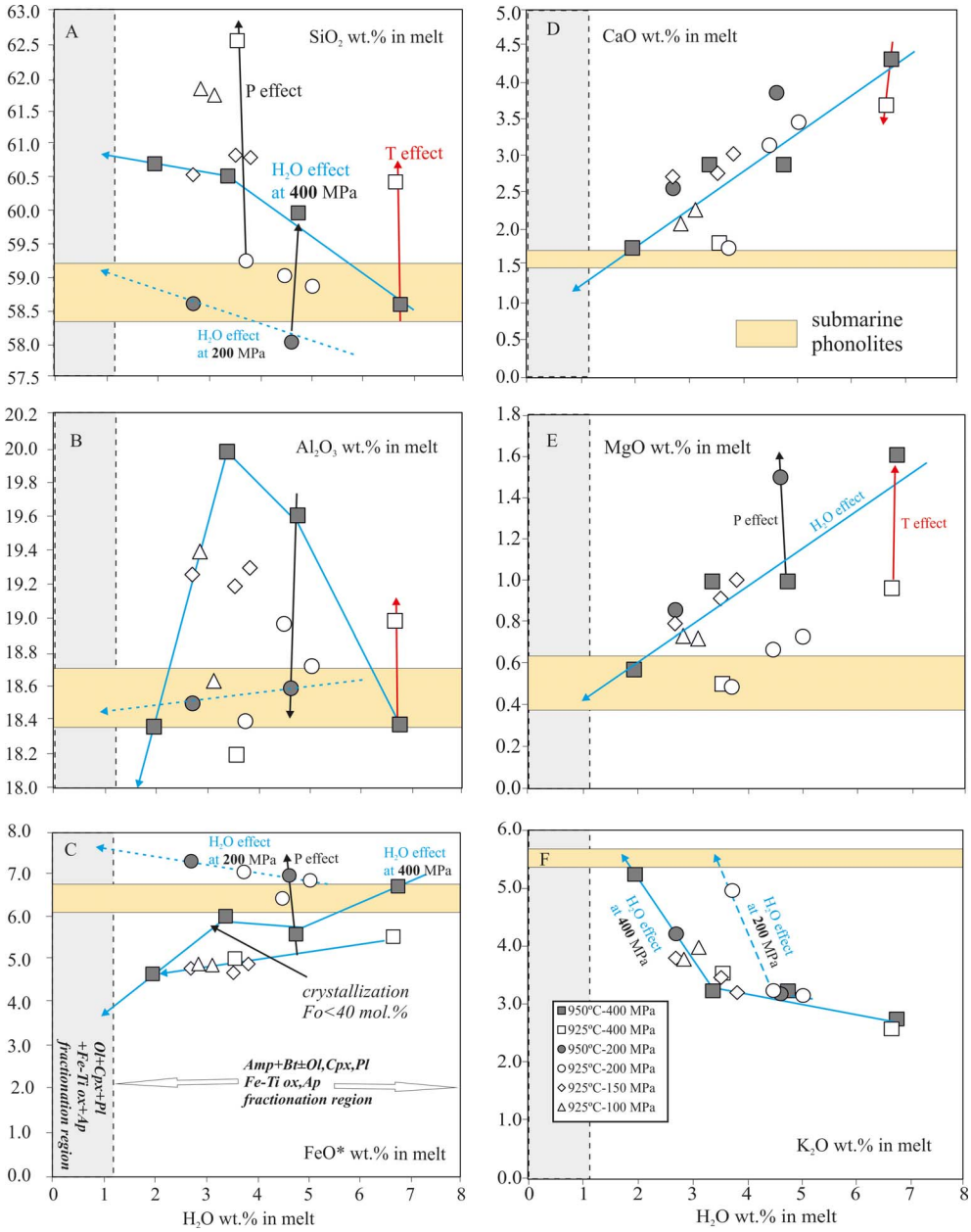

Figure 8. Experimental glass compositional variations of major and minor oxides versus H_2O_{melt}. For each graph, the yellow horizontal bar shows the natural compositions of phonolites dredged on the Horseshoe site (Table 1). Grey vertical bar shows the fractionation region for Ol+Cpx+Mt+Ilm+Ap (see text for details). Vertical errors equal the symbol sizes.

4.3.6. *Experimental glasses*

Residual glass compositions (calculated on a 100% anhydrous basis) have benmoreitic–trachytic affinities (according to the classification of Le Bas and Streckeisen [1991] with P.I. (peralkaline indice, =Na+K/Al in moles) at 0.7–1 (Figures 8–9, Table 9). Only charges DR08-143 and DR08-131 produced

liquids that straddle the phonolite–trachyte boundary line (Figure 9), having a P.I. = 0.95–1, normative nepheline (6.5–7%) and containing 2–4 wt% H_2O_{melt} (Table 8). The production of benmoreitic–trachytic–phonolitic liquids reflects the significant degree of crystallization of the charges. In the range of temperatures explored in this work, crystallization is dominated by Amp+Bt along with different proportions of Fe–Ti oxides+Ap for H_2O_{melt} in the range 2–7 wt% (Figures 3–4, Table 2). The onset of Pl+Ol+Cpx crystallization results in a drastic decrease of Mt, Amp and Bt proportions until the breakdown of the two last phases which occurs at ≤2 wt% H_2O_{melt} (Figure 3). The combination of the above factors increases both the SiO_2 and the alkalinity of the residual melt, which reaches the phonolitic field (Figure 9A). In parallel, TiO_2 (not shown), CaO and MgO decrease (Figure 8B,D). In contrast, FeO* may even slightly increase when H_2O_{melt} decreases (Figure 8C), though by a modest amount (usually <0.5 wt%). This Fe-enrichment is due to the changing proportions of hydrous Fe–Mg phases and Mt (Table 2). In comparison, a decrease of 200 MPa lowers FeO* by ~1.5–2 wt% for a given H_2O_{melt} (Figure 8C). Below 3 wt% H_2O_{melt}, the liquid produced at 400 MPa are even more depleted in FeO* (Figure 8C). This is due to the fact that, at 200 MPa, the precipitation of a relatively Fe-poor Ol (Fo_{45-40}) enhances the iron-enrichment process. In contrast, at 400 MPa, the crystallization of significant amounts of relatively fayalitic-rich Ol (e.g., Fo ≤ 38) counteracts the depleting role of Mt at higher H_2O_{melt} (Figures 3, 8C). Such a difference explains why charges at 200 MPa yield melts with the highest analyzed FeO* contents (7.4 wt%) compared to their high-pressure counterparts, which achieved only a maximum of 6.7 wt% FeO*, and under very high H_2O_{melt}.

Another striking point concerns the charges annealed at 100–150 MPa since these yield residual melt compositions overlaping those produced at higher P (≥200 MPa), not only in terms of iron but also in the other major elements (Figure 8). In fact, despite the presence of moderate proportions of olivine with compositions Fo_{51-43} (Figure 5A, Table 3), which according to 200 MPa data promotes the Fe-enrichment of the melt, the co-crystallization of ~8 wt% of Fe-rich magnetite and different amounts of Cpx+Pl±Bt±Amp inhibit the Fe-enrichment process and drive the residual melt towards more Si- and Al-rich and low P.I. compositions [Figures 8–9; Table 8; Botcharnikov et al., 2008, Giehl et al., 2013, Scaillet and MacDonald, 2006, Toplis and Carroll, 1995]. The effect of P variation is not restricted to FeO*; as pressure increases, the SiO_2, CaO increase with decreasing Al_2O_3 content, MgO and alkalis being somewhat less affected (Figure 8).

It should be also noted that between 7 and 3 wt% H_2O_{melt}, the precipitation of Amp along with Bt in amounts, representing 60–80% of the total crystal cargo, increases the SiO_2 and Al_2O_3 content but buffers K_2O at ~3 wt% (Figure 8F). Below this H_2O_{melt}, the crystallization of Ol+Cpx+Pl, along with a drastic drop of Amp+Bt+Mt proportions, increases the potassium content of the melt by ~50% relative (Figure 8F). Na_2O follows a similar trend but the observed enrichment is less significant compared to K_2O. The evolution of Al_2O_3 is well illustrated in series run at 200–400 MPa where Al_2O_3 increases when H_2O_{melt} decreases until the onset of Pl crystallization (Figure 8B). Pl crystallization in relative high proportions (up to ~30 wt%; Table 2) decreases the Al_2O_3 and accelerates the evolution of the residual melts towards alkali-rich compositions.

Aside from water and pressure, temperature is also an important parameter controlling melt composition. At lower temperatures (i.e. 925 °C) and for a fixed H_2O_{melt}, residual liquids tend to be enriched in SiO_2 and Na_2O but depleted in TiO_2, MgO and CaO when compared to melts produced at 950 °C. FeO*, K_2O and Al_2O_3 do not show any clear relationship with T in charges run at P ≤ 200 MPa. Only those at 400 MPa and 950 °C have higher Al_2O_3 and FeO compared to their colder counterparts (Figure 8).

In summary, the fractionation of a relatively hydrous basanite under low oxygen fugacity conditions (fO_2 ≤ FMQ; Table 2), at temperatures between 925–950 °C and 200–400 MPa (corresponding to depths of 6–12 km) produces Fe-rich phonolitic liquids containing 2–4 wt% dissolved H_2O. In the next section, we use the composition of the natural phonolites dredged along the Mayotte submarine ridge or collected on-land to shed light on the conditions needed to generate this type of evolved melts at Mayotte.

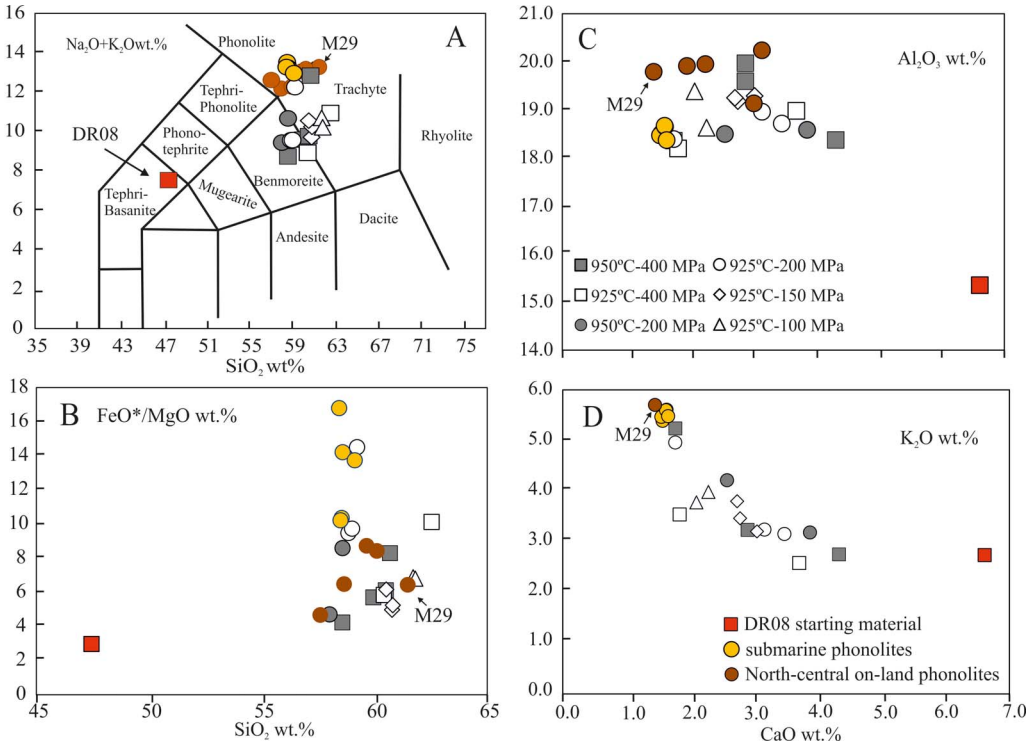

Figure 9. (A) Total alkalis ($Na_2O + K_2O$) versus SiO_2 diagram [after Le Bas and Streckeisen, 1991] showing the composition of the experimental glasses, the DR08 starting material, and onland/offshore phonolites at Mayotte (Table 1). (B) FeO*/MgO versus. SiO_2 wt%, (C) Al_2O_3 versus CaO wt%, (D) K_2O versus CaO wt%. Legend as in previous figures. Vertical errors are equal to symbol size.

5. Discussion

As stated in the previous sections, most of the seismo-volcanic activity recorded during the 2018–2021 eruptive episode (and up to date) occurred along the 60 km long submarine volcanic ridge located eastward of Mayotte (Figure 1B). Dredged samples along this ridge define a bimodal distribution of basanites and phonolites [Berthod et al., 2021a,b], phonolites mostly outcropping in the Horseshoe region (Figure 1). Submarine mafic magmas are chemically and petrologically similar to the on-land counterparts from the moderately silica-undersaturated Comoros chemical trend [Bachèlery et al., 2016, Berthod et al., 2021b, Pelleter et al., 2014]. Dredged phonolites have major and trace elements that are also compatible with this magmatic lineage. However, when compared to their on-shore equivalents, they are slightly enriched in Fe–Mg–Ca and have lower Al-total alkalis content, both akin to the somewhat less evolved character of these magmas [Pelleter et al., 2014]. This is also reflected by differences between submarine and on-shore phonolites in their mineralogy. Whereas offshore phonolites are moderate porphyritic magmas with small crystals (≤200 µm) of fayalitic Ol (Fo ≤ 32 mol%), Pl (An ≤ 24 mol%), Ap and Fe–Ti oxides microcrystals [Ox; Berthod et al., 2021b], those on land are characterized by the presence of an amphibole-bearing assemblage consisting of Cpx+Amp+Afs+Ap+Ox±nepheline (Nph) [Debeuf, 2004, Pelleter et al., 2014]. It is worth noting that Ol-bearing phonolites are not restricted to the submarine domain since they were also identified onshore at Mayotte [Berthod et al., 2021b, Debeuf, 2004]. Based on our experimental results, the differences in phase assemblage and composition observed between these two groups can potentially be related to changes in the evolution conditions of the parental basanitic magma (P–T–H_2O), as we discuss below.

5.1. *Production of phonolitic liquids at the WNW–ESE submarine volcanic ridge of Mayotte*

The low porphyritic character of the submarine phonolites dredged in the vicinity of the active Horseshoe structure of Mayotte [Berthod et al., 2021a,b] allows us to consider the bulk-rock composition as representative of liquids. Accordingly, the experimental results detailed above are useful for understanding the conditions for the production of phonolitic melts at this site (Figures 8–9, Tables 1 and 8). Although glasses produced at conditions of 925 °C–200 MPa and 950 °C–400 MPa with 2–7 wt% H_2O_{melt} broadly reproduce the SiO_2, Al_2O_3, MgO and CaO contents of natural phonolites (Figure 8), only the residual glasses of charges DR08-143 (950 °C–400 MPa; ~2 wt% H_2O_{melt}) and DR08-131 (925 °C–200 MPa; ~4 wt% H_2O_{melt}) closely match the phonolitic affinities (P.I. ~ 0.9–1) of the natural products (Figure 9A; Table 1). Both charges have the same mineral assemblage and phase proportions (~65 wt% of Ol+Pl+Amp+Mt+Ilm+Ap±Bt; Table 2), but differ in the composition of the phases (see above). In detail, only the 200 MPa experiment closely reproduces the FeO* and SiO_2 contents (and other oxides) as well as the FeO*/MgO ratios (Figure 9B). The glass produced at 400 MPa has a FeO* content ~2 wt% lower and a higher SiO_2 with respect to the dredged phonolites (Figure 9B). Our data therefore show that the crystallization of DR08 basanite at 925 °C–200 MPa (corresponding to depths of 6–8 km) and under relatively reduced conditions (fO_2 ~ FMQ; Table 2) generates phonolitic melts (with up to 3.8 wt% H_2O_{melt}) with FeO* contents and FeO*/MgO ratios similar to phonolites sampled offshore. Whereas such T–P–H_2O_{melt} estimates are in agreement with the conditions set for most of the phonolites and evolved peralkaline magmas worldwide [Andújar et al., 2008, 2010, 2013, Andújar and Scaillet, 2012, Di Carlo et al., 2010, Giehl et al., 2013, Moussallam et al., 2013, Romano et al., 2018, Scaillet and MacDonald, 2006, Scaillet et al., 2008], they strongly differ from those inferred by Berthod et al. [2021b], in particular with respect to pressure conditions: as stated previously, these authors conclude that the fractionation of a 80 wt% dry mineral assemblage from a hydrous basanite (2.3 wt% H_2O_{melt}) at mantle depths (18–20 km, 600 MPa) produces the Fe-rich phonolites of the ridge. However, in this model, no role is given to the hydrous phases like amphibole or biotite in the evolutionary process. Assuming that H_2O_{melt} (2.3 wt%) determined in olivine melt inclusions in DR08 sample by Berthod et al. [2021b] is representative, a fractionating assemblage lacking Amp with such an H_2O_{melt} requires a maximum pressure of ~200 MPa (Figure 3). Our results show, however, that basanite crystallization under such wet conditions (i.e., ending with residual liquids with H_2O_{melt} > 6 wt%, as required by the largely incompatible behaviour of H_2O, for 80 wt% crystallization of a basanite with 2.3 wt% H_2O_{melt}) produces mostly trachytic melts (Figure 9A), true phonolites requiring drier conditions (<3–4 wt%). This mismatch is seemingly due to the fact that MELTs does not incorporate amphibole, which is an important fractionating phase in hydrous basanite as our experiments demonstrate.

It should be also stressed here that the differences between MELTs calculations and our results not only concern the role of hydrous phases in the fractionating process, but also the composition of feldspar that is in equilibrium with these Fe-rich phonolitic melts. Whereas the calculations of Berthod et al. [2021b] predict the precipitation of at least 30% of alkali feldspar (anorthoclase) to produce the phonolitic melts, the experimental charges yielding to such type of liquids are instead characterized by the presence of relatively primitive Plagioclase (oligoclase) with composition ~27 mol% in the fractionating mineral assemblage. The submarine phonolites have a dominant alkali feldspar population at ≤An_{15} mol%, but also contain a few more calcic cores (An_{24} mol%) [Berthod et al., 2021b]. The latter is close to that of experimental Pl ($An_{27\pm3}$ mol%) produced in charge DR08-131 (925 °C–200 MPa), which is as shown above, in equilibrium with a Mayotte-type phonolitic liquid. Hence, the more calcic Pl cores in the natural phonolite can be considered as crystals inherited from the fractionation process involving the crystallization of the mineral assemblage Ol+Pl+Amp+Mt+Ilm+Ap±Bt down to the phonolitic production stage. The less calcic and dominant variety of feldspar microphenocrysts in the phonolite is likely the result of a small increment of crystallization that occurred after the phonolitic liquid was extracted from its parental basanitic magma, perhaps due to an adiabatic cooling effect upon

decompression that took place when the phonolitic melt had left the basanitic reservoir.

Hence, we conclude that conditions of 950/925 °C–200 MPa with H_2O_{melt} ≤ 3–4 wt% are best suited for the production of Fe-rich phonolites at Mayotte. Deeper conditions produce significantly different compositions, as stated previously (Figure 8).

5.2. *The production of the north-central Mayotte Karthala type phonolites*

As stated in previous sections, the compositions of the magmas at Mayotte clearly define two distinct magmatic series. Since our starting basanitic composition belongs to the moderate-silica undersaturated series (i.e. Karthala type), our results primarily apply to this specific compositional lineage (Figure 2).

Detailed mineralogical information concerning the phonolitic products of Mayotte is scarce, however: only the works of Pelleter et al. [2014] and Späth et al. [1996] provide bulk-rock information and few mineral data from these evolved compositions (Table 1). For comparison purposes, we have only considered the bulk-rock compositions having MgO contents up to 0.4 wt%, since these are the maximum amounts of our experimental melts (Table 8). The phonolites-trachytes with MgO contents lower than ~0.25 wt% represent the most evolved products of the Karthala LLD [Pelleter et al., 2014, Späth et al., 1996]. In this case, the liquids produced in our experiments possibly represent the parental compositions from which the Mayotte on-land phonolites derive.

Compared to phonolites from the submarine ridge, those from Mayotte island are characterized by a contrasted mineralogy [Amp+Cpx+Mt+Ilm+Afs+Ap±Nph) and have slightly lower Fe-contents (between 3.7 to 5.1 wt%; Pelleter et al., 2014]. Rare Ol+Afs bearing phonolites [i.e., equivalent to the dredged products; Berthod et al., 2021b], and aphyric glassy samples [sample M29 in Pelleter et al., 2014; Table 1] can be also found in the northern-central parts of Mayotte.

Apart from sample M29, the Mayotte phonolites are reproduced by the 200–400 MPa series products on TAS, FeO*/MgO, CaO, Al_2O_3 versus SiO_2 Harker diagrams (Figure 9), suggesting that these melts could have been potentially generated at ~300 MPa (9 km depth). This pressure is about 100 MPa (3 km) higher (deeper) than that determined for the conditions of production of their 2018–2021 submarine equivalents. However, both the lower iron content of the Mayotte island phonolites compared to the submarine ridge products and the presence of Amp in these compositions (Amp stability is enhanced with pressure; Figure 3), support deeper conditions for generation of the on-land phonolites.

The M29 aphyric sample has the highest SiO_2 (61.5 wt%) and the lowest FeO* (3.2 wt%) contents of all phonolites considered in this work (Table 1). According to our results, the production of this phonolitic composition will require ponding conditions of a DR08 type basanite at pressures ≥400 MPa. In fact, the melt from the charge DR08-143 run at 400 MPa closely matches the total alkalis and SiO_2 contents of this phonolite (Figure 9A). However, when it comes to FeO*/MgO ratio and TiO_2 and CaO contents, the best fits are obtained by charges produced at 925 °C–100 MPa (Figure 9, Table 8). The absence of phenocrysts in the natural sample does not allow us to use the mineralogical information to discriminate between these conditions. However, we cannot exclude that this aphyric phonolite was produced by the fractionation of a basanitic magma at low-pressure (≤100 MPa) and under relatively dry (≤3 wt%) and hot (?) conditions.

As stated above, the existence of phonolites, with MgO contents <0.4 wt% containing a mineral assemblage Amp+Cpx+Pl+Fe–Ti oxides [Debeuf, 2004, Pelleter et al., 2014], suggests that, even if these magmas evolved from liquids similar to those produced in this work, their composition and mineralogy [low-Mg number of amphiboles, Debeuf, 2004] do not necessary reflect the production level: they could reflect shallower final ponding conditions. This observation highlights the need for detailed petrographic data on Mayotte phonolites, especially those on-land, if we are to define more precisely the pre-eruptive conditions of Khartala-type phonolites.

5.3. *Various levels of phonolite production/storage at Mayotte*

The crystallization experiments, performed on a representative evolved basanitic sample from the 2018–2021 eruption, allowed us to define the best conditions (T–P–fO_2–fH_2O) for producing the characteristical compositional variability of phonolites

from the north-central parts of the Grand Terre island, Petite Terre and NE active submarine ridge of Mayotte. In particular, these experiments show the ease of producing phonolitic melts in the shallow crust, as observed in many other settings. Phonolitic melts containing up to ~3–4 wt% of H_2O_{melt} are produced by the extensive crystallization of at least 65 wt% of a mineral assemblage consisting of Ol+Pl+Amp+Cpx+Bt+Mt+Ilm+Ap, at crustal levels ≤12–15 km. Pressure (hence depth) appears to be an important factor controlling the final FeO* content of residual phonolitic liquids. This oxide could be potentially used as a geobarometer (for this type of magma series) to infer the generation/storage depths of corresponding magmas.

A conceptual model summarizing our view on Mayotte phonolites is shown in Figure 10. Considering the above water-contents, the differentiation of basanitic magmas at depths ≤4–5 km produces residual liquids with trachyte–benmoreite affinities. The Fe-enriched phonolite compositions found in the Mayotte system are instead produced at around 6–8 km, whereas at greater depths, the fractionation process results in the generation of phonolitic melts which are progressively enriched in SiO_2–Al_2O_3 and depleted in FeO*.

Hence, the production of phonolitic melts with the Karthala affinities of Mayotte island occurs at multiple depths above the local Moho [16–17 km, Dofal et al., 2021]. However, the presence of highly evolved phonolitic magmas (i.e. MgO poor) suggests that these magmas experienced a later episode of crystallization and fractionation at shallower levels, prior to their eruption. The occurrence of relatively shallow phonolitic reservoirs below the Horseshoe region (Figure 1C) would have permitted their subsequent rapid emptying and collapse during past eruptions, which would readily explain the presence of a caldera-looking depression at this point, since relatively shallow depths of magma reservoirs favors the formation of caldera structures [e.g. Martí et al., 2008].

Our results contrast with the conditions inferred from mineral geobarometers and MELTS simulations, which for producing the Fe-rich phonolites from Mayotte, predict the crystallization of a dry mineral assemblage at significantly higher pressures than those determined in this work (600 versus 200 MPa). This difference highlights the still poor resolution that these two methods have for predicting the depths of magma evolution in alkaline systems, and calls for additional calibration of these tools.

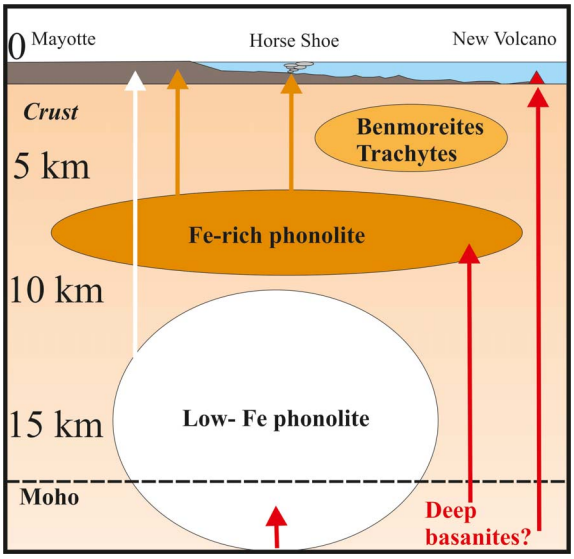

Figure 10. Conceptual model of the plumbing system operating at Mayotte for producing Fe-rich, Low-Fe phonolites and benmoreite–trachyte compositions (see text for details). Moho location from Dofal et al. [2021].

Conflicts of interest

Authors have no conflict of interest to declare.

Acknowledgments

The authors thank Patricia Benoist for the technical support with SEM and EMPA. We thank the scientific party of the MAYOBS 2 (DR08 sampling) campaign that was conducted by several French research institutions and laboratories (IPGP/CNRS/BRGM/IFREMER/IPGS). All marine operations are performed as part of the MAYOBS set of campaigns (https://doi.org/10.18142/291), under the supervision of REVOSIMA (Réseau de Surveillance Volcanologique et Sismologique de Mayotte; REVOSIMA), a partnership between the Institut de Physique du Globe de Paris (IPGP), the Institut Français de Recherche pour l'Exploitation de la Mer (IFREMER), the Bureau de Recherches Géologiques

et Minières (BRGM), the Centre National de la Recherche Scientifique (CNRS) and the REVOSIMA consortium. We thank the captain and crew of the R/V Marion Dufresne (TAAF/IFREMER/LDA). R. Cioni and an anonymous reviewer are thanked for the detailed reviews of this work. We want also to thank the editorial handling of editor Jérôme Van der Woer.

Funding

This work was supported by the Institut des Sciences de la Terre d'Orléans (ISTO-CNRS), the LABEX VOLTAIRE (ANR-10-LABX-100-01) and the EQUIPEX PLANEX (11-EQPX-0036). Since June 2019, all activities on Mayotte, including MAYOBS campaigns, are funded by le Ministère de l'Enseignement Supérieur, de la Recherche et de l'Innovation (MESRI), le Ministère de la Transition Ecologique (MTE), le Ministère des Outremers (MOM), le Ministère de l'Intérieur (MI), and le Ministère des Armées with the support of the DIRMOM (Direction Interministérielle aux Risques Majeurs en Outremer) and the MAPPPROM (Mission d'appui aux politiques publiques pour la prévention des risques majeurs en Outremer).

Supplementary data

Supporting information for this article is available on the journal's website under https://doi.org/10.5802/crgeos.182 or from the author.

References

Andersen, D. J. and Lindsley, D. H. (1998). Internally consistent solution models for Fe–Mg–Mn–Ti oxides: Fe–Ti oxides. *Am. Mineral.*, 73, 714–726.

Andújar, J., Costa, F., and Martí, J. (2010). Magma storage conditions of the last eruption of Teide volcano (Canary Islands, Spain). *Bull. Volcanol.*, 72, 381–395.

Andújar, J., Costa, F., Martí, J., Wolff, J. A., and Carroll, M. R. (2008). Experimental constraints on pre-eruptive conditions of phonolitic magma from the caldera-forming El Abrigo eruption, Tenerife (Canary Islands). *Chem. Geol.*, 257, 173–191.

Andújar, J., Costa, F., and Scaillet, B. (2013). Storage conditions and eruptive dynamics of central versus flank eruptions in volcanic islands: the case of Tenerife (Canary Islands, Spain). *J. Volcanol. Geotherm. Res.*, 260, 62–79.

Andújar, J., Martel, C., Pichavant, M., Samaniego, P., Scaillet, B., and Molina, I. (2017). Structure of the plumbing system at Tungurahua volcano, Ecuador: Insights from phase equilibrium experiments on July–August 2006 eruption products. *J. Petrol.*, 58, 1249–1278.

Andújar, J. and Scaillet, B. (2012). Experimental constraints on parameters controlling the difference in the eruptive dynamic of phonolitic magmas: the case from Tenerife (Canary Islands). *J. Petrol.*, 53, 1777–1806.

Andújar, J., Scaillet, B., Pichavant, M., and Druitt, T. H. (2015). Differentiation conditions of a basaltic magma from Santorini, and its bearing on the production of andesite in arc settings. *J. Petrol.*, 56, 765–794.

Bachèlery, P., Morin, J., Villeneuve, N., Soulé, H., Nassor, H., and Ali, A. R. (2016). Structure and eruptive history of Karthala volcano. In *Active Volcanoes of the Southwest Indian Ocean*, pages 345–366. Springer-Verlag, Berlin and Heidelberg.

Berndt, J., Holtz, F., and Koepke, J. (2001). Experimental constraints on storage conditions in the chemically zoned phonolitic magma chamber of the Laacher See Volcano. *Contrib. Mineral. Petrol.*, 140, 469–486.

Berndt, J., Koepke, J., and Holtz, F. (2005). An experimental investigation of the influence of water and oxygen fugacity on differentiation of MORB at 200 MPa. *J. Petrol.*, 46, 135–167.

Berthod, C., Médard, E., Bachèlery, P., Gurioli, L., Di Muro, A., Peltier, A., Komorowski, J., Benbakkar, M., Devidal, J., Langlade, J., Besson, P., Boudon, G., Rose-Koga, E., Deplus, C., Le Friant, A., Bickert, M., Nowak, S., Thinon, I., Burckel, P., Hidalgo, S., Jorry, S., Fouquet, Y., and Feuillet, N. (2021a). The 2018-ongoing Mayotte submarine eruption: magma migration imaged by petrological monitoring. *Earth Planet. Sci. Lett.*, 571, article no. 117085.

Berthod, C., Médard, E., Di Muro, A., Hassen Ali, T., Gurioli, L., Chauvel, C., Komorowski, J.-C., Benbakkar, M., Devidal, J.-L., Besson, P., Le Friant, A., Deplus, C., Nowak, S., Thinon, I., Burckel, P., Hidalgo, S., Feuillet, N., Jorry, S., and Fouquet, Y. (2021b). Mantle xenolith-bearing phonolites and basanites feed the active volcanic ridge of Mayotte

(Comoros archipelago, SW Indian Ocean). *Contrib. Mineral. Petrol.*, 176(10), 1–24.

Bertil, D., Mercury, N., Doubre, C., Lemoine, A., and Van Der Woerd, J. (2021). The unexpected Mayotte 2018–2020 seismic sequence: a reappraisal of the regional seismicity of the Comoros. *C. R. Géosci.*, 353, 211–235.

Botcharnikov, R. E., Almeev, R. R., Koepke, J., and Holtz, F. (2008). Phase relations and liquid lines of descent in hydrous ferrobasalt-implications for the Skaergaard intrusion and Columbia river flood basalts. *J. Petrol.*, 49, 1687–1727.

Burnham, C. W., Holloway, J. R., and Davis, N. F. (1969). *Thermodynamic Properties of Water to 10000 °C and 10,000 Bars*, volume 132. Geological Society of America Publ., Special Paper No. 132.

Cesca, S., Letort, J., Razafindrakoto, H. N. T., Heimann, S., Rivalta, E., Isken, M. P., Nikkhoo, M., Passarelli, L., Petersen, G. M., Cotton, F., and Dahm, T. (2020). Drainage of a deep magma reservoir near Mayotte inferred from seismicity and deformation. *Nat. Geosci.*, 13, 87–93.

Chou, I.-M. (1978). Calibration of oxygen buffers at elevated P and T using the hydrogen fugacity sensor. *Am. Mineral.*, 63, 690–703.

Dautria, J. M., Girod, M., and Rahaman, O. (1983). The upper mantle beneath eastern Nigeria: inferences from ultramafic xenoliths in Jos and Biu volcanics. *J. African Earth Sci.*, 1, 331–338.

Debeuf, D. (2004). *Étude de l'évolution volcano-structurale et magmatique de Mayotte (archipel des Comores, océan Indien)*. PhD thesis, Université de la Reunion.

Deer, W. A., Howie, R. A., and Zussman, J. (1972). *Rock-Forming Minerals, Volume 4: Framework Silicates*. Longmans, Green and Co. Ltd., London.

Di Carlo, I., Pichavant, M., Rotolo, S. G., and Scaillet, B. (2006). Experimental crystallization of a High-K arc basalt: the golden pumice, Stromboli volcano (Italy). *J. Petrol.*, 47, 1317–1343.

Di Carlo, I., Rotolo, S. G., Scaillet, B., Buccheri, V., and Pichavant, M. (2010). Phase equilibrium constraints on pre-eruptive conditions of recent felsic explosive volcanism at Pantelleria Island, Italy. *J. Petrol.*, 51, 2245–2276.

Dofal, A., Fontaine, F. R., Michon, L., Barruol, G., and Tkalcic, H. (2021). Nature of the crust beneath the islands of the Mozambique channel: Constraints from receiver functions. *J. African Earth Sci.*, 184, article no. 104379.

Erdmann, S., Martel, C., Pichavant, M., and Kushnir, A. (2014). Amphibole as an archivist of magmatic crystallization conditions: problems, potential, and implications for inferring magma storage prior to the paroxysmal 2010 eruption of Mount Merapi, Indonesia. *Contrib. Mineral. Petrol.*, 167, article no. 1016.

Feuillet, N. (2019). MAYOBS1 cruise, RV Marion Dufresne. https://doi.org/10.17600/18001217.

Feuillet, N., Jorry, S., Crawford, W., Deplus, C., Thinon, I., Jacques, E., Saurel, J.-M., Lemoine, A., Paquet, F., Satriano, C., Aiken, C., Foix, O., Kowalski, P., Laurent, A., Rinnert, E., Cathalot, C., Donval, J. P., Guyader, V., Gaillot, A., Scalabrin, C., Moreira, M., Peltier, A., Beauducel, F., Grandin, R., Ballu, V., Daniel, R., Pelleau, P., Gomez, J., Besançon, S., Géli, L., Bernard, P., Bachèlery, P., Fouquet, Y., Bertil, D., Lemarchand, A., and Van der Woerd, J. (2021). Birth of a large volcanic edifice offshore Mayotte via lithosphere-scale dyke intrusion. *Nat. Geosci.*, 14(10), 787–795.

Foix, O., Aiken, C., Saurel, J. M., Feuillet, N., Jorry, S. J., Rinnert, E., and Thinon, I. (2021). Offshore Mayotte volcanic plumbing revealed by local passive tomography. *J. Volcanol. Geotherm. Res.*, 420, article no. 107395.

Freise, M., Holtz, F., Nowak, M., Scoates, J. S., and Strauss, H. (2009). Differentiation and crystallization conditions of basalts from the Kerguelen large igneous province: an experimental study. *Contrib. Mineral. Petrol.*, 158, 505–527.

Ghiorso, M. S. and Gualda, G. A. R. (2015). An H_2O-CO_2 mixed fluid saturation model compatible with rhyolite-MELTS. *Contrib. Mineral. Petrol.*, 169, 1–30.

Giehl, C., Marks, M., and Nowak, M. (2013). Phase relations and liquid lines of descent of an iron-rich peralkaline phonolitic melt: an experimental study. *Contrib. Mineral. Petrol.*, 165, 283–304.

Gualda, G. A. R., Ghiorso, M. S., Lemons, R. V., and Carley, T. L. (2012). Rhyolite-MELTS: a modified calibration of MELTS optimized for silica-rich, fluid-bearing magmatic systems. *J. Petrol.*, 53, 875–890.

Hammer, J., Jacob, S., Welsch, B., Hellebrand, E., and Sinton, J. (2016). Clinopyroxene in postshield Haleakala ankaramite: 1. Efficacy of thermobarom-

etry. *Contrib. Mineral. Petrol.*, 171, article no. 7.

Harms, E., Gardner, J. E., and Schmincke, H. U. (2004). Phase equilibria of the lower Laacher See Tephra (East Eifel, Germany): constraints on pre-eruptive storage conditions of a phonolitic magma reservoir. *J. Volcanol. Geotherm. Res.*, 134, 135–148.

Iacovino, K., Oppenheimer, C., Scaillet, B., and Kyle, P. (2016). Storage and evolution of mafic and intermediate alkaline magmas beneath Ross Island, Antarctica. *J. Petrol.*, 57, 93–118.

Jiménez-Mejías, M., Andújar, J., Scaillet, B., and Casillas, R. (2021). Experimental determination of H_2O and CO_2 solubilities of mafic alkaline magmas from Canary Islands. *C. R. Géosci.*, 353, 289–314.

Jorry, S. J. (2019). MAYOBS2 cruise, RV Marion Dufresne. https://doi.org/10.17600/18001222.

Klügel, A., Albers, E., and Hansteen, T. H. (2022). Mantle and crustal xenoliths in a tephriphonolite from La Palma (Canary Islands): implications for phonolite formation at oceanic island Volcanoes. *Front. Earth Sci.*, 10, article no. 761902.

Klügel, A., Schmincke, H. U., White, J. D. L., and Hoernle, K. A. (1999). Chronology and volcanology of the 1949 multi-vent rift-zone eruption on La Palma (Canary Islands). *J. Volcanol. Geotherm. Res.*, 94, 267–282.

Laurent, A., Satriano, C., and Bernard, P. (2021). Accurate depth determination of VLF events of the ongoing seismo-volcanic crisis in Mayotte. In *5èmes Rencontres Scientifiques et Techniques Résif, Nov 2021 Obernai (67210), France*. https://hal.archives-ouvertes.fr/hal-03481002. HAL Id: hal-03481002.

Lavayssière, A., Crawford, W. C., Saurel, J.-M., Satriano, C., Feuillet, N., Jacques, E., and Komorowski, J.-C. (2022). A new 1D velocity model and absolute locations image the Mayotte seismo-volcanic región. *J. Volcanol. Geotherm. Res.*, 421, article no. 107440.

Le Bas, M. J. and Streckeisen, A. L. (1991). The IUGS systematics of igneousrocks. *J. Geol. Soc. Lond.*, 148, 825–833.

Lemoine, A., Briole, P., Bertil, D., Roullé, A., Foumel, M., Thinon, I., Raucoules, D., de Michele, M., and Valty, P. (2020). The 2018–2019 seismo-volcanic crisis east of Mayotte, Comoros islands: seismicity and ground deformation markers of an exceptional submarine eruption. *Geophys. J. Int.*, 223(1), 22–44.

MacDonald, R., White, J. C., and Belkin, H. E. (2021). Peralkaline silicic extrusive rocks: magma genesis, evolution, plumbing systems and eruption. *C. R. Géosci.*, 353, 7–59.

Martí, J., Geyer, A., Folch, A., and Gottsmann, J. (2008). Chapter 6. A Review on collapse caldera modelling. In Gotssmann, J. and Martí, J., editors, *Caldera Volcanism, Analysis, Modelling and Respons*, Developments in Volcanology, page 492. Elsevier, Amsterdam, the Netherlands.

Moussallam, Y., Oppenheimer, C., Scaillet, B., and Kyle, P. R. (2013). Experimental phase-equilibrium constraints on the phonolite magmatic system of Erebus Volcano, Antarctica. *J. Petrol.*, 54, 1285–1307.

Nehlig, P., Lacquement, F., Bernard, J., Caroff, M., Deparis, J., Jaouen, T., Pelleter, A. A., Perrin, J., Prognon, C., and Vittecoq, B. (2013). Notice de la carte géologique de Mayotte. BRGM/RP-61803-FR, 135 p., 45 ill., 1 ann.

Neumann, E.-R., Wulff-Pedersen, E., Johnsen, K., Andersen, T., and Krogh, E. (1995). Petrogenesis of spinel harzburgite and dunite suite xenoliths from Lanzarote, eastern Canary Islands: implication for the upper mantle. *Lithos*, 35, 83–107.

Pedrazzi, D., Cerda, D., Geyer, A., Martí, J., Aulinas, M., and Planagumà, L. (2022). Stratigraphy and eruptive history of the complex Puig de La Banya del Boc monogenetic volcano, Garrotxa volcanic field. *J. Volcanol. Geotherm. Res.*, 423, article no. 107460.

Pelleter, A. A., Caroff, M., Cordier, C., Bachelery, P., Nehlig, P., Debeuf, D., and Arnaud, N. (2014). Melilite-bearing lavas in Mayotte (France): An insight into the mantle source below the Comores. *Lithos*, 208–209, 281–297.

Pownceby, M. I. and O'Neill, H. St. C. (1994). Thermodynamic data redox reactions at high temperatures. III. Activity-composition relations in Ni-Pd alloys from EMF measurements at 850–1250 K and calibration of the NiO + Ni–Pd assemblage a redox sensor. *Contrib. Mineral. Petrol.*, 116, 327–339.

Putirka, K. D. (2008). Thermometers and barometers for volcanic systems. *Rev. Mineral. Geochem.*, 69, 61–120.

Putirka, K. D. (2016). Amphibole thermometers and barometers for igneous systems and some implications for eruption mechanisms of felsic magmas at arc Volcanoes. *Am. Mineral.*, 101, 841–858.

ReVoSiMa (2022). Bulletin no 39 de l'activité sismo-volcanique à Mayotte, du 1er au 28 fevrier 2022. http://www.ipgp.fr/sites/default/files/ipgp_revosima_n39_20220304.pdf. ISSN: 2680-1205.

Ridolfi, F. (2021). Amp-TB2: an updated model for calcic amphibole thermobarometry. *Minerals*, 11(3), article no. 324.

Robie, R. A., Hemingway, B. S., and Fisher, J. R. (1979). Thermodynamic properties of minerals and related substances at 298.15 K and 1 bar (105 pascals) pressure and at higher temperatures. *US Geol. Surv. Bull.*, 1452.

Romano, P., Andújar, J., Scaillet, B., Romengo, N., Di Carlo, I., and Rotolo, S. G. (2018). Phase equilibria of Pantelleria Trachytes (Italy): constraints on pre-eruptive conditions and on the Metaluminous to Peralkaline transition in silicic magmas. *J. Petrol.*, 59, 559–588.

Saurel, J. M., Retailleau, L., Weiqiang, Z., Issartel, S., Satriano, C., and Beroza, G. C. (2021). Implementation of a new real time seismicity detector for the Mayotte crisis. EGU21-10646. https://doi.org/10.5194/egusphere-egu21-1-10646.

Scaillet, B. and MacDonald, R. (2006). Experimental constraints on pre-eruption conditions of pantelleritic magmas: evidence from the Eburru complex, Kenya Rift. *Lithos*, 91, 95–108.

Scaillet, B., Pichavant, M., and Cioni, R. (2008). Upward migration of Vesuvius magma chamber over the past 20,000 years. *Nature*, 455, 216–219.

Scaillet, B., Pichavant, M., and Roux, J. (1995). Experimental crystallization of leucogranite magmas. *J. Petrol.*, 36, 663–705.

Scaillet, B., Pichavant, M., Roux, J., Humbert, G., and Lefévre, A. (1992). Improvements of the Shaw membrane technique for measurement and control of fH2 at high temperatures and pressures. *Am. Mineral.*, 77, 647–655.

Späth, A., Roex, A. P. L., and Duncan, R. A. (1996). The geochemistry of lavas from the Comores Archipelago, Western Indian Ocean: petrogenesis and mantle source region characteristics. *J. Petrol.*, 37, 961–991.

Toplis, M. J. and Carroll, M. R. (1995). An experimental study of the influence of oxygen fugacity on feti oxide stability, phase relations, and mineral-melt equilibria in ferro-basaltic systems. *J. Petrol.*, 36, 1137–1170.

Ubide, T., Mollo, S., Zhao, J., Nazzari, M., and Scarlato, P. (2019). Sector-zoned clinopyroxene as a recorder of magma history, eruption triggers, and ascent rates. *Geochim. Cosmochim. Acta*, 251, 265–283.

Webster, J. D., Holloway, J. R., and Hervig, R. L. (1987). Phase equilibria of a Be, U and F-enriched vitrophyre from Spor Mountain, Utah. *Geochim. Cosmochim. Acta*, 51, 389–402.

Wolff, J. A. (1985). Zonation, mixing and eruption of silica-under-saturated alkaline magma: a case study from Tenerife, Canary1986 Mount St. Helens eruptions. *J. Geophys. Res.*, 98, 19667–19685. Islands. Geol. Mag., 122, 623–640.

Zinke, J., Reijmer, J. J. G., Thomassin, B. A., Dullo, W.-C., Grootes, P. M., and Erlenkeuser, H. (2003). Postglacial flooding history of Mayotte lagoon (Comoro archipelago, southwest Indian Ocean). *Mar. Geol.*, 194, 181–196.